Growth Signaling Autonomy in Circulating Tumor Cells Aids Metastatic Seeding

Saptarshi Sinha[1], Alex Farfel[2], Kathryn E. Luker[2], Barbara A. Parker[4,5], Kay Yeung[4,5], Gary D. Luker[6-8]* and Pradipta Ghosh[1,5,9]*

Affiliations:

[1]Department of Cellular and Molecular Medicine, School of Medicine, University of California San Diego, La Jolla, CA 92093.

[2]Biointerfaces Institute, University of Michigan.

[4]Moores Cancer Center, University of California San Diego, La Jolla, CA 92093.

[5]Department of Medicine, School of Medicine, University of California San Diego, La Jolla, CA 92093.

[6]Department of Biomedical Engineering, University of Michigan, 109 Zina Pitcher Place, Ann Arbor, MI, 48109-2200, USA.

[7]Department of Microbiology and Immunology, University of Michigan, 109 Zina Pitcher Place, Ann Arbor, MI, 48109-2200, USA

[8]Center for Molecular Imaging, Department of Radiology, University of Michigan, 109 Zina Pitcher Place, Ann Arbor, MI, 48109-2200, USA

[9]Veterans Affairs Medical Center, La Jolla, CA.

***Corresponding authors**:

Gary D. Luker, M.D; Professor, Radiology, Biomedical Engineering and Microbiology and Immunology, A524 BSRB 109 Zina Pitcher Place, Ann Arbor, MI 48109-2200; Phone: 734-764-2890; Email: gluker@med.umich.edu

Pradipta Ghosh, M.D.; Professor, Departments of Medicine and Cellular and Molecular Medicine, University of California San Diego; 9500 Gilman Drive (MC 0651), George E. Palade Bldg, Rm 232, 239; La Jolla, CA 92093. Phone: 858-822-7633. Email: prghosh@ucsd.edu.

Keywords: Cellular Autonomy; GIV; Girdin; CCDC88A; metastasis, mesenchymal-epithelial transition (MET); Epithelial-mesenchymal transition (EMT); Epithelial mesenchymal plasticity

Abstract (limit: 250; current: 227)

Self-sufficiency (autonomy) in growth signaling, the earliest recognized hallmark of cancer, is fueled by the tumor cell's ability to 'secrete-and-sense' growth factors; this translates into cell survival and proliferation that is self-sustained by auto-/paracrine secretion. A Golgi-localized circuitry comprised of two GTPase switches has recently been implicated in the orchestration of growth signaling autonomy. Using breast cancer cells that are either endowed or impaired (by gene editing) in their ability to assemble the circuitry for growth signaling autonomy, here we define the transcriptome, proteome, and phenome of such autonomous state, and unravel its role during cancer progression. We show that autonomy is associated with enhanced molecular programs for stemness, proliferation, and epithelial-mesenchymal plasticity (EMP). Autonomy is both necessary and sufficient for anchorage-independent growth factor-restricted proliferation and resistance to anti-cancer drugs and is required for metastatic progression. Transcriptomic and proteomic studies show that autonomy is associated, with a surprising degree of specificity, to self-sustained EGFR/ErbB signaling. Derivation of a gene expression signature for autonomy revealed that growth signaling autonomy is uniquely induced in circulating tumor cells (CTCs), the harshest phase in the life of tumor cells when it is deprived of biologically available EGF. We also show that autonomy in CTCs tracks therapeutic response and prognosticates outcome. These data support a role for growth signaling autonomy in multiple processes essential for the blood-borne dissemination of human breast cancer.

46 **GRAPHIC ABSTRACT:**

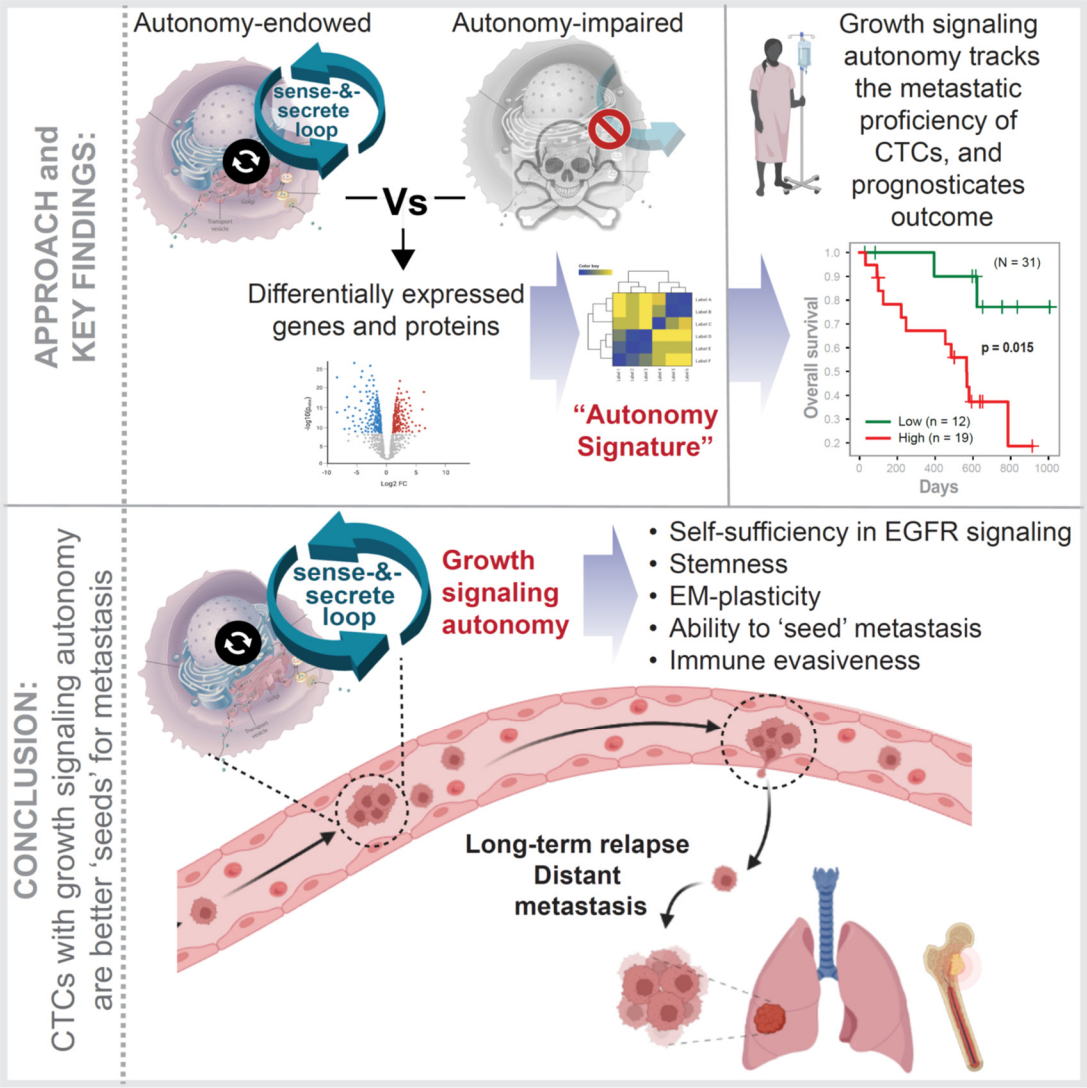

47

48

49 **Significance Statement** (limit: 120; current: 120)

50 A Golgi-localized molecular circuitry has been recently implicated in the orchestration of secrete-and-
51 sense auto-/paracrine loops that impart self-sufficiency in growth signaling, a.k.a., growth signaling
52 autonomy. Using a transdisciplinary approach, this work shows that growth signaling autonomy is
53 uniquely induced in tumor cells that are in circulation. Circulating tumor cells (CTCs) represent a brutish
54 and risky phase in the lifetime of tumor cells when they are exposed to the immune system and
55 hemodynamic sheer forces, all in the setting of growth factor starvation. Cancer cells appear to rely on
56 the autonomy circuit to survive and enhance their fitness to seed metastases. Autonomy generates the
57 kind of 'eat-what-you-kill' entrepreneurial spirit which minimizes the risk of CTCs dying on an otherwise
58 risky journey.
59

60 Main Text

61 **Introduction**

62 Metastatic breast cancer (MBC) remains a fatal disease. While ~5-10% of patients are diagnosed with
63 MBC at initial diagnosis, ~20-30% of patients with stage I-III breast cancer will eventually recur with MBC.
64 Hence, understanding which cells 'seed' metastases in MBC is of paramount importance to improve the
65 management and outcome of these patients.

66 Metastasis begins with the intravasation of cancer cells from primary tumors, either as single cells
67 or in clusters, into the systemic circulation. These circulating tumor cells (CTCs) must then extravasate
68 from the blood stream and disseminate to distant tissues, where they either remain dormant or give rise
69 to metastases (1-3). However, for CTCs to 'seed' metastases, they must survive despite the loss of
70 anchorage to the matrix, exposure to the immune system and hemodynamic shear forces. The past two
71 decades has witnessed significant technological leaps to help detect, enumerate, and characterize CTCs
72 [reviewed in (4, 5)]. Numerous correlations have been discovered between CTCs and the ability to initiate
73 metastases: abundance (6), phenotypic properties, e.g., enhanced protein translation (7), proliferation
74 (7, 8), epithelial-mesenchymal plasticity (9-11), epithelial-type CTCs [with restricted mesenchymal
75 transition (7, 12)] that assemble junctions and circulate as clusters (13-16), CTC ½ life (17), the presence
76 of platelets (15) and immune cells [such as neutrophils (8)] in those clusters, hypoxia (18) and circadian
77 rhythm [nighttime worse than day (19)]. Despite these insights, mechanisms connecting these diverse
78 phenotypes to drive aggressive features of CTCs remain unknown. While clustering, either homotypic,
79 with each other, or heterotypic with platelets provide explanation for how CTCs protect themselves from
80 shear forces and evade the immune system, little to nothing is known about how they survive the journey
81 in the face of a precipitous drop in growth factors. For example, the concentration of EGF within primary
82 tumors and xenografts range from ~1–2 ng/ml (20); however, serum EGF levels range between ~13-14
83 pg/ml (21). Of the detectable EGF in serum, most of it is biologically inactive and is associated with
84 platelets (22), which is released during the process of coagulation (23). In fact, EGF is virtually
85 undetectable in plasma that is collected in the presence of inhibitors of coagulation (24).

86 It is perhaps because of these adversities that the process by which CTCs initiate metastases is
87 highly inefficient [2.7% efficiency, as determined using MBC-patient derived CTCs in xenotransplantation
88 models (25)], implying that only a fraction of CTCs--the fittest of them all--are endowed with tumorigenic
89 and metastatic functionality. What signaling mechanisms and/or molecular machineries impart or
90 maintain CTC fitness in growth factor-deprived state remains a hot topic of debate, and objective
91 molecular measurements of the metastatic potential of CTCs remains an unattainable Holy Grail of
92 precision medicine.

Here we report the serendipitous discovery of a distinct CTC phenotype, i.e., growth signaling autonomy that is induced in CTCs, but not in primary tumors or established metastases. Growth signaling autonomy, or self-sufficiency in growth factor (GF) signaling, is the first of the six hallmarks of all cancers to be defined (26), and yet remains one of the least well understood. Many cancer cells synthesize growth factors (GFs) to which they are responsive, creating a positive feedback signaling loop called autocrine stimulation (27). In fact, serum-free cell culture studies squarely implicate autocrine secretion of growth factors as key support for intracellular mechanisms that impart autonomy [reviewed in (28)]. Recently, using an integrated systems and experimental approach, a molecular circuit has been described which is critical for multiscale feedback control to achieve secretion-coupled autonomy in eukaryotic cells (29). This circuit is comprised of two species of GTPases, monomeric Arf1 and the heterotrimeric Gi, coupled by the multi-modular scaffold GIV, (i.e., *G*α-*i*nteracting *v*esicle associated protein; aka Girdin; gene *CCDC88A*) within a closed-loop circuit that is localized at the Golgi (29, 30) Coupling is initiated only when cells are subjected to restricted growth factor conditions. Coupling within such a closed-loop control system generates two emergent properties: (i) dose-response alignment behavior of sensing and secreting growth factors; and (ii) multiscale feedback control to achieve secretion-coupled growth and survival signaling (31). Consequently, cells with a coupled circuit are self-sufficient in growth signaling, i.e., autonomous, and can survive and achieve homeostasis in GF-restricted conditions; cells in which the circuit is uncoupled (as in GIV-KO cells) are not.

In this work, we provide evidence for the requirement of such autonomy in breast cancer CTCs and reveal the biological implications and translational potential of our observations.

114 **Results**

115

116 *Study design*

117 To study how autonomy in cancer cells impact cancer progression, and more specifically, breast cancers,
118 we took the advantage of two MDA MB-231 breast cancer cell lines, that are either endowed (WT) or
119 impaired (GIV-KO by CRISPR (29)) in growth signaling autonomy (**Fig 1a**). We focused on these cells
120 because they are a highly aggressive, invasive, and poorly differentiated triple-negative breast cancer
121 (TNBC) cell line which lacks the estrogen receptor (ER), progesterone receptor (PR), as well as
122 amplification of the HER2 (human epidermal growth factor receptor 2) receptor and is one of the triple-
123 negative basal subtype cell line most widely used in metastatic breast cancer research (32) (40.2% of
124 total PubMed citations). It is also a cell line that has been shown to require GIV for growth signaling
125 autonomy (29). We analyzed these cells by functional and 'omics'-based approaches to navigate the
126 uncharted territory of cancer cell autonomy. Because the GTPase circuit for autonomy requires GIV's
127 modules/motifs that evolved only in the higher eukaryotes (29), and GIV is overexpressed in most cancers
128 (33), we hypothesized that tumor cells may frequently assemble and utilize such an evolutionary
129 advantage to achieve growth signaling autonomy at some stage during cancer progression. Using an
130 integrated computational and experimental approach, we systematically analyzed these pair of cell lines
131 for key hallmarks of cancer cells.

132

133 *Growth signaling autonomy is associated with stemness and epithelial-mesenchymal plasticity.*

134 The expression of *CCDC88A* gene (which encodes GIV) was significantly upregulated when the
135 autonomous WT, but not GIV-KO cells were switched from 10% to 0% serum conditions (**Fig 1b**), which
136 is consistent with the increased need for autocrine growth factor signaling during serum starvation
137 (absence of exogenous growth factors, i.e., 0% FBS). Although conventional markers of normal
138 pluripotent stem cells remained unchanged during serum depravation in both cells (**Fig 1c**), markers of
139 cancer stem cells (CSCs) followed the same pattern as *CCDC88A* (**Fig 1d**). When we analyzed the core
140 pluripotency master regulators (the Yamanaka factors (34); **Fig 1e**) and the breast cancer-specific indices
141 of the degree of oncogenic dedifferentiation (identified using a machine learning algorithm (35)) (**Fig 1f**),
142 the autonomous WT cells maintained these signatures despite serum depravation; GIV-KO cells did not.
143 These patterns (induction or maintenance in the autonomous WT, but suppression in GIV-KO cells) were
144 observed repeatedly across a comprehensive panel of gene signatures of breast cancer aggressiveness
145 and stemness that have been reported in the literature (**Fig 1g**; **Figure S1**).

146 Autonomous WT, but not GIV-KO cells also induced gene signatures for epithelial-mesenchymal
147 plasticity (EMP (36)), i.e., the ability of cells to interconvert between epithelial and mesenchymal
148 phenotypes in response to signals (**Fig 2**). For example, all gene signatures derived from isolated distinct
149 single-cell clones from the SUM149PT human breast cell line spanning the E↔EM1-3↔M1-2 spectrum,
150 previously characterized for diverse migratory, tumor-initiating, and metastatic qualities (37), were
151 induced in the autonomous WT, but suppressed in the GIV-KO cells during serum depravation (**Fig 2a-**
152 **b**). Acquisition of EMP plasticity in MDA-MB-231 cells under conditions of serum deprivation is
153 remarkable since these cells typically show a highly mesenchymal phenotype(38). An identical pattern
154 was seen also for the transcriptional census of EMP in human cancers, which was derived by leveraging
155 single-cell RNA seq data from 266 tumors spanning 8 different cancer types (39) (**Fig 2c**). This held true
156 for both the 328-gene EMP consensus signature (**Fig 2d**), as well as its cancer cell-specific 128-gene
157 subset (**Fig 2e**). Furthermore, numerous gene signatures across the EMT and MET spectrum, derived
158 from diverse human samples representing the stages of metastasis (primary tumors, CTCs, and
159 metastases) and genes that are essential for establishing cell-cell junctions were induced in the
160 autonomous WT, but remained unchanged or were suppressed in the GIV-KO cells (**Fig S2**).
161 These findings indicate that GIV-dependent growth signaling autonomy is required to support
162 molecular programs of stemness and EMP in growth factor-restricted conditions (i.e., 0% FBS); however,
163 such autonomy is largely dispensable in the presence of excess growth factors because all readouts
164 were indistinguishable when WT and KO cells were compared at 10% FBS (**Fig 1-2**).
165
166 *Autonomy is required for anchorage-independent growth and metastatic spread.*
167 We next assessed if the autonomy-endowed and -impaired cells are capable of anchorage-independent
168 growth, which is a hallmark of anoikis resistance and the path to further steps in metastasis (40). When
169 tested for growth as spheroids in soft agar at varying serum concentrations, while both WT and GIV-KO
170 cells did so in the presence of excess serum, only the autonomous WT cells thrived in serum-restricted
171 conditions (0.2% FBS; **Fig 3a-c**). Under serum-restricted growth conditions, the autonomous WT, but not
172 the autonomy-impaired GIV-KO cells were also relatively resistant to various classes of conventional
173 chemotherapeutic agents that are typically used to treat TNBCs (e.g., anthracyclines, alkylating agents),
174 as determined by the observed differences in their half-maximal inhibitory concentrations (IC_{50}; **Fig 3d**).
175 Compared to the KO cells, the autonomous WT cells also displayed significantly higher metastatic
176 potential after intracardiac injection (**Fig 3e-f**). Notably, WT and GIV-KO cells produced comparable
177 metastases when cells were cultured in complete serum prior to intracardiac injection (compare WT and
178 KO, 10% FBS; **Fig 3f**). These findings indicate that GIV is required for 3D growth, chemoresistance and

179 metastasis in serum-restricted conditions and that GIV-dependent growth signaling autonomy may be
180 required for these phenotypes.
181 Previous work has documented the absence of full-length GIV in MCF7 cells, the most widely used
182 ER-positive breast cancer cell line (43.6% of total PubMed citations(32)). These MCF7 cells depend on
183 the growth hormone estrogen to proliferate. We found that restoring GIV expression in these cells using
184 a Tol2-based transposon vector was sufficient to enable estrogen-independent growth, as determined
185 using the ER-antagonist Fulvestrant (**Fig S3a-b**) and Tamoxifen **Fig S3b**). GIV was also sufficient for the
186 growth of MCF7 as spheroids in soft agar under estrogen- and serum-restricted conditions (0.2%; **Fig**
187 **S3c-d**). This impact of GIV on cell growth/survival in serum-restricted conditions was limited to growth
188 factors and hormone, but not for the CDK4/6 inhibitor, Palbociclib (**Fig S3b**), a commonly used
189 therapeutic agent in metastatic ER+ breast cancers, which blocks the cell cycle transition from G1 to S
190 by inhibiting the kinase activity of the CDK/cyclin complex. Findings suggest that GIV-dependent growth
191 signaling autonomy may be sufficient for growth factor and hormone-restricted growth.
192
193 *'Autonomy' represents a distinct cell state that is self-sufficient in EGFR/ErbB growth signaling.*
194 RNA sequencing studies revealed a set of 30 genes (27 up- and 3 downregulated) and two miRNAs were
195 most differentially expressed (DEGs; Log fold change >5; **Fig 4a**; **Supplemental Information 3**) between
196 the autonomous WT and the GIV-KO cells. These genes were up- and downregulated in WT and KO
197 cells, respectively, in response to serum depravation (**Fig 4b**), a pattern that was strikingly similar to
198 those observed previously for signatures of stemness (**Fig 1g**) and EMP (**Fig 2a-e**). No genes were
199 significantly differentially expressed between the two cell lines when cultured in 10% serum. The list of
200 upregulated DEGs was notable for the presence of EGF (**Fig 4c**); a reactome pathway analysis confirmed
201 that this list was significantly enriched in genes that participated in the EGFR/ErbB-signaling pathway
202 (**Fig 4d**). Pathway analysis of the downregulated DEGs was notable for cellular processes related to the
203 extracellular matrix (ECM), e.g., collagen formation, assembly, and degradation, activation of
204 metalloproteinases and degradation of ECM (**Fig S4**).
205 Using the composite score of expression of the 30 genes as a signature of growth signaling
206 autonomy (henceforth, "Autonomy signature") we navigated a wide range of cellular stress response
207 states to assess specificity to growth-factor deprivation (as opposed to non-specific 'stress response').
208 The autonomy signature was induced in MDA MB-231 cells challenged with serum deprivation (**Fig S5c**)
209 but not glucose deprivation, oxidative stress, hypoxia, ER-stress, or mechanical compression (**Fig 4e**;
210 **Fig S5c-i**). The signature was suppressed in HeLa cells undergoing anastasis, a process of resurrection
211 in which cancer cells can revive after ethanol-induced apoptosis (**Fig S5a-b**; **Fig 4e**). Furthermore, the
212 autonomy signature had no overlaps with other signatures that are either approved for clinical use by the

213 FDA or in clinical trial for their utility in the management of breast cancers (**Fig S5j**). Together, these
214 findings indicate that the gene set of growth signaling autonomy are unique; they represent a distinct
215 'cellular state' that is induced under serum-restricted conditions and requires GIV.

216 Tandem Mass Tag (TMT)-based quantitative proteomics studies (**Fig 4f**) revealed that that
217 autonomous WT cells differential express a distinct set of proteins, which included EGFR (2.308-fold;
218 **Supplemental Information 4**). When we constructed a protein-protein interaction (PPI) network using
219 this list of upregulated proteins fetched from the human interactome (see network edges in
220 **Supplemental Information 5**), EGFR emerged as the node with highest degree of connectivity (**Fig 4g-**
221 **h; Supplemental Information 6**). The most connected proteins (i.e., nodes of the PPI network with Z_d
222 >= 3) that are upregulated in autonomous WT cells were, once again, found to be significantly enriched
223 in proteins that participate in the EGFR/ErbB2 signaling pathway (**Fig 4i**).

224 Thus, the transcriptomic and proteomic studies agree; both reveal an upregulated EGFR/ErbB2
225 signaling pathway in the autonomous WT cells during serum-restricted conditions and confirm the
226 requirement of GIV in such upregulation. Intriguingly, both *EGF* gene and EGFR protein emerged from
227 these 'omics' studies, with an enrichment of its immediate downstream signaling (e.g., signaling via Grb2,
228 PLCγ, CDC42, Rho and Rac GTPases), and both secretory and endocytic trafficking proteins (e.g.,
229 COP1, RABs, SNARE, EXOC1 ARF6, AP2-subunits, CAV1 proteins; **Fig 4h**). Findings show that the
230 transcriptome and proteome of growth signaling autonomy supports both auto-/paracrine secretion and
231 signaling within the EGFR/ErbB pathway. They also provide a gene signature for growth signaling
232 autonomy, which is exclusively induced on-demand during scarcity of resources.
233

234 *Growth signaling autonomy is induced in CTCs.*

235 Next, using the newly derived autonomy signature as a computational tool, we sought to navigate the
236 various steps within the cancer initiation and progression cascade. A microarray dataset generated using
237 xenografts of MDA MB-231 cells implanted into inguinal and axillary fat pads of NOD scid female mice,
238 which included samples representing all major steps of the cascade was prioritized (see **Fig 5a**-*left*). To
239 our surprise, the autonomy signature was neither induced in primary tumors, nor in metastases; it was
240 induced exclusively in CTC isolated from blood samples (**Fig 5a**-*right*). Findings in mice were conserved
241 in humans; the autonomy signature was induced in human CTCs (**Fig 5b**) but not in human primary
242 tumors (when compared to normal, across all molecular subtypes; **Fig S5k**). When primary tumors from
243 patients with detectable CTCs were compared to those without, the autonomy signature was higher in
244 tumors that shed CTCs (**Fig 5c**). Although this degree of specificity (for CTCs) was surprising, that the
245 autonomy signature was induced in CTCs is consistent with the near total lack of biologically active EGF
246 in serum (see *Introduction*).

247 Next, we interrogated diverse human CTC datasets that were generated by independent groups, in
248 which the metastatic proficiency of the CTCs was experimentally validated using xenograft models. For
249 example, intratumoral hypoxia is a known driver of intravasation of clustered CTCs with high metastatic
250 proficiency (18). We found the autonomy signature significantly higher in hypoxic clusters of live CTCs
251 were compared against their normoxic counterparts (**Fig 5d**), all drawn from a breast cancer patient and
252 labeled with HypoxiaRed, a cell-permeable dye that tags hypoxic cells based on their nitroreductase
253 activity (18). The shedding of CTCs is known to peak at the onset of night (41), when they display more
254 metastatic proficiency (19). It is also known that compared to single CTCs, the metastatic proficiency of
255 CTC clusters (15) and CTC-WBC clusters (8) are higher. The autonomy signature was induced in
256 CTC/CTC-WBC clusters (compared to single CTCs; **Fig 5e**); the significance of such induction was
257 higher in CTC-WBC clusters that were collected at night (**Fig 5e**).
258
259 *Autonomy signature in CTCs tracks therapeutic response and prognosticates outcome.*
260 CTCs exhibit dynamic changes in abundance and epithelial and mesenchymal composition during
261 treatment (10); we asked if/how treatment might impact the autonomy signature. We analyzed a dataset
262 comprised of CTCs serially collected during a previously published study on an index patient (**Fig 5f**-*left*),
263 which displayed reversible shifts between these compositions accompanying each cycle of response to
264 therapy (R) and disease progression (P). The autonomy signature was rapidly downregulated (alongside
265 CTC count) during treatment initiation, which coincided with therapeutic response (1-3 mo.; **Fig 5f**-*right*).
266 The signature was subsequently induced from 3rd-7th month (despite continuation of treatment and low
267 CTC counts) and preceded clinically confirmed disease progression at the 8th mo. which necessitated
268 salvage chemotherapy (**Fig 5f**-*right*). The signature did not show any discernible relationship with the
269 relative amounts of E/M compositions, which is in keeping with our prior observation that autonomy is
270 associated with EM-plasticity (**Fig 2**).
271 We next re-analyzed a single-cell RNA seq dataset generated using 135 viable CTC samples,
272 from 31 unique patients with hormone receptor positive MBC, for whom follow-up and outcome data were
273 available (overall survival, as updated on 2/10/2020 (7)). CTCs were freshly isolated directly from whole
274 blood using a CTC-iChip microfluidic device (42) (**Fig 5g**-*left*). A Kaplan-Meier survival analysis revealed
275 a higher 3-year mortality risk among those with high autonomy signature in CTCs compared to those with
276 low expression of the same (p=0.015; **Fig 5g**-*right*).

277 *Autonomy is associated with the potential to re-epithelialize, evade the immune system, and proliferate.*
278 CTCs must display plasticity between epithelial and mesenchymal states to complete the metastatic
279 process (10), and the EGF/EGFR pathway has been identified as 1 of the 14 major pathways that support
280 EM-plasticity (39). We asked if the self-sustained EGF/EGFR signaling program in autonomy is
281 specifically associated with 'reversibility' of the EMT process. We took advantage of a dataset in which
282 Her2-transformed human mammary epithelial (HMLE) cells were either programmed for reversible EMT
283 (induced by TGFβ) or to a stable mesenchymal phenotype (by chronic exposure to the ErbB inhibitor,
284 lapatinib) (**Fig 6a**). Xenograft studies using these programmed cells had confirmed that reversible, but
285 not stable mesenchymal phenotype produces long-bone metastases (43). We found the autonomy
286 signature to be higher in cells programmed for reversible EMT compared to both stable mesenchymal
287 cells and established bone metastases (**Fig 6b**). This indicates that the autonomous state is present in
288 transformed cells that carry the potential to undergo dynamic transitions (EM-plasticity) but is lost when
289 cells get stuck in either stable mesenchymal (as during the emergence of resistance to Lapatinib) or re-
290 epithelialized states (as in established metastatic colonies).
291 EMT and stemness in tumor cells correlate with immune checkpoint expression and complex
292 interactions with platelet and immune cells (35, 44); similarly, the metastatic proficiency of the CTCs is
293 regulated by interactions with the platelets and immune cells (45). We found that all major CTC markers
294 that are known to be critical for the assembly of the CTC-monocyte (**Fig 6c-d**), the CTC-platelet (**Fig 6e-**
295 **f**; **Fig S6a-f**) and the CTC-NK cell (**Fig 6g-h**) synapses were expressed at significantly higher levels in
296 the autonomous WT cells compared to their GIV-KO counterparts exclusively in 0% FBS conditions.
297 These findings suggest that autonomous WT, but not the autonomy-impaired GIV-KO cells are likely to
298 be able to mount an immune evasion ["do not eat me"] response by escaping phagocytosis by monocytes,
299 triggering platelet aggregation and activation which shields CTCs from NK cells, and finally, evading
300 cytolytic killing by NK cells.
301 Besides immune evasion, CTC-neutrophil interactions are known to induce the expression of CTC
302 genes that outline cell cycle progression, leading to more efficient metastasis formation (45). This
303 neutrophil-related pro-proliferative signature was highly expressed in the autonomous WT cells but
304 suppressed in the autonomy-impaired GIV-KO cells upon serum deprivation (**Fig 6i-j**). A similar pattern
305 was seen also for the universal proliferation marker gene, MKI67 (**Fig 6k**), and two other gene sets [Gene
306 Set Enrichment Analysis (GSEA)] for cell cycle progression, KEGG and BIOCARTA (**Fig S6g-h**).
307 These findings suggest that the autonomous state in serum-restricted condition is associated with
308 three key CTC properties that are essential for metastasis, i.e., plasticity, immune evasion, and
309 proliferative potential.
310 **Discussion**

311 In this work, we validate a model system for studying one of the hallmarks of cancers, i.e., self-sufficiency
312 in growth signaling or growth signaling autonomy, define the transcriptome, proteome, and phenome of
313 such autonomous state, and unravel its role during cancer progression. Findings show that the
314 autonomous state is prominently induced in a subset of CTCs and empower them with key properties
315 which may make them better 'seeds' for metastasis (see **Fig 7**). Elaborated below are the three major
316 implications of these findings.
317
318 **The autonomous state embodies key features of CTCs that confer metastatic potential.**
319 We found that the autonomous state that is unique to a subset of CTCs supports a gene expression
320 program for stemness (i.e., oncogenic de-differentiation), proliferation, immune evasiveness, and EM-
321 plasticity. Of these features, the most distinct one is EMP, because much like what we see in the case of
322 growth signaling autonomy, EMP is unique to CTCs and very rare in primary tumor cells or in metastases
323 (46). Autonomy is reduced/lost in cells that are unable to transition between E↔M states. These findings
324 are in keeping with the gathering notion that CTCs are the metastatic precursors that simultaneously
325 express epithelial and mesenchymal markers and best display dynamic E→M and M→E transitions (10).
326 Such a hybrid state in which CTCs have acquired only a partial mesenchymal state allows rapid E→M
327 transitions needed to migrate and intravasate, and quick M→E reversals to reinitiate a tumor at a distant
328 site (47). Consequently, epithelial-type CTCs with a restricted mesenchymal transition initiate metastases
329 efficiently, whereas mesenchymal-type CTCs don't (12). Consistent with prior findings that CTC clusters
330 express cell-cell adhesion proteins that are components of tight junctions and desmosomes (15, 48), we
331 show that the autonomous state is endowed with gene expression program to support tight junctions
332 (which are essential for the formation of CTC clusters). Divergent from classical EMT, EM-plasticity is
333 known to also induce unique immunomodulatory effects (49, 50); consistent with this notion, our model
334 was also accompanied by a diverse array of immune-evasion machinery. Because EM-plasticity has
335 been broadly implicated in metastasis, chemoresistance and immunosuppression (51), and is present in
336 autonomy-endowed cells that outperformed autonomy-impaired cells in their ability to initiate metastases
337 in mice, we conclude that autonomy-endowed CTCs are likely to be more efficient in seeding metastases
338 than those CTCs that are autonomy-impaired.
339 Mechanistically, growth signaling autonomy is supported by a secretion-coupled sensing circuit
340 at the Golgi apparatus (29, 30) which controls the secretory flux and organelle shape (compact vs
341 fragmented stacks when the circuit is enabled or disabled, respectively). These findings are in keeping
342 with prior work showing that CTC population level behavior is dominated by a few high-secreting cells
343 (52), and that Golgi shape (fragmentation vs compact) is a strong correlate of CTC-EMT and invasiveness

344 (53). Although it remains unknown if/how the Golgi-resident circuit begets EM-plasticity, we conclude that
345 growth signaling autonomy and phenotypic plasticity, two hallmarks of cancer, co-exist in CTCs.
346
347 **Autonomous CTCs support a self-sufficient EGFR/ErbB signaling program.**
348 Our transcriptomic and proteomic analyses pinpointed with surprising convergence that the autonomous
349 state supports a self-sufficient EGFR/ErbB-centric signaling program in the absence of external growth
350 factors. While most cells can be stimulated by growth factors made by neighboring cells—via the process
351 of paracrine signaling—many cancer cells acquire self-sufficiency such that they sense and respond to
352 what they synthesize and secrete, creating a positive feedback sense-and-secrete loop known as
353 autocrine stimulation (54). Such a type of self-sufficiency or autonomy in a cancer cell obviates its need
354 to depend exclusively on the surroundings, especially during the intravascular journey (when CTCs
355 cannot access biologically active EGF) and during the initial phase of avascular growth of a CTC that has
356 just extravasated to a new site. Although examples of such autonomy exist in the case of PDGF and
357 TGFα by glioblastomas and sarcomas, respectively, and MDA MB-231 cells are known to secrete
358 EGF(55), autocrine autonomy in the EGF/EGFR pathway has not been described previously and
359 mechanisms that support such sense-and-secrete loops in eukaryotes had remained elusive. By
360 demonstrating that a secretion-coupled-sensing machinery at the Golgi (29, 30) that requires scaffolding
361 by GIV is essential for tumor cells to achieve a state of self-sufficiency in EGFR/ErbB signaling, it is not
362 unusual for us to find that such a state is endowed with a multitude of pro-oncogenic biological processes
363 that are known to be supported by EGFR/ErbB signals, including cell anchorage-independent cell growth,
364 stemness, EM-plasticity and metastasis (56). Findings are also in keeping with prior observation of *EGFR*
365 gene induction in EMT that is accompanied by plasticity and tumorigenicity (but not in EMT alone (57)).
366 Although it remains unclear if our findings are related to the previously reported prognostic roles of high
367 EGFR (58, 59) and Her2 (60) in the serum of patients with breast cancers, EGFR/ErbB2 has been
368 detected in CTCs consistently during serial blood draws (61) and was found to be activated (as
369 determined by the presence of its phosphorylated state (62) in CTCs) with increasing frequency often
370 during MBC progression (62). Because inhibition of EGFR prevents CTC clustering and diminishes
371 metastatic potential (63), it is possible that higher autonomy observed in the CTC-clusters (compared to
372 single-CTCs) requires the autonomous signaling machinery (the sense-and-secrete loop) for CTCs to
373 remain clustered and maintain metastatic potential. It is possible that the EGF-predominant autocrine
374 loop maintains CTC-junctions within clusters by triggering both the secretion of junctional
375 proteins/complexes (e.g., E-cadherin) from the Golgi to the plasma membrane (PM) (64) and their
376 subsequent activation at the junctions (65).
377

Autonomy signature could identify CTCs that are the 'fittest' precursors to metastases.

In the absence of available tools to objectively assess, report and track the metastatic potential of CTCs, their use in prognosticating risk of relapse or to track the emergence of therapeutic resistance in real-time and adapt the clinical response has yet to be realized. We show that a gene signature for growth signaling autonomy can track treatment response in a single index patient, and more importantly, the signature prognosticates outcome in a dataset of 31 unique patients. Molecular markers of the metastatic potential of CTCs have been described before, e.g., RPL15 (7) and a 17-gene signature (66). While RPL15 was identified during an *in vivo* genome-wide CRISPR activation screen to identify genes in breast cancer patient-derived CTCs that promote their distant metastasis in mice, the latter was trained on a cohort of normal vs primary tumor and whole blood from patients. Unlike both these instances, in which investigative approaches were geared to identify CTC-specific markers, we stumbled upon the autonomy signature as a portal into the metastatic proclivity of CTCs by serendipity, using the gene expression signature for autonomy. Regardless, of how it was identified, our findings not only add growth signaling autonomy to the growing list of the parameters that help define the 'fitness' of CTCs, but also provide a methodology to objectively measure (using a gene signature) the degree of autonomy (and hence, the fitness) of CTCs to serve as 'seeds' for metastases. Prospective studies are required to further investigate the clinical utility of this signature.

In conclusion, our work provides insights into what determines the success of a CTC to serve as metastatic "seed". By demonstrating that the detached tumor cells (*sans* ECM contact) gain autocrine self-sufficiency in growth factor signaling and phenotypic plasticity in circulation, while maintaining the properties of stemness, proliferation and immune evasiveness (which are seen also in primary tumors), we show the coexistence of two hallmarks of cancer that are relatively unique to CTCs and are intricately intertwined.

402 **Materials and Methods**

403

404 **EXPERIMENTAL METHODS**

405 **Cell lines**

406 MDA-MB-231 cells were grown at 37°C in their suitable media, according to their supplier instructions,
407 supplemented with 10% FBS, 100 U/ml penicillin, 100 µg/ml streptomycin, 1% L-glutamine, and 5%
408 CO2.GIV knock-out (KO) cell lines were generated using Pooled guide RNA plasmids (commercially
409 obtained from Santa Cruz Biotechnology; Cat# sc-402236-KO-2), as described earlier(67). Briefly, these
410 CRISPR/Cas9 KO plasmids consist of GFP and Girdin-specific 20 nt guide RNA sequences derived from
411 the GeCKO (v2) library and target human Girdin exons 6 and 7. Plasmids were transfected into Hela and
412 MDA-MB-231 cells using PEI. Cells were sorted into individual wells using a cell sorter based on GFP
413 expression. To identify cell clones harboring mutations in gene coding sequence, genomic DNA was
414 extracted using 50 mM NaOH and boiling at 95°C for 60mins. After extraction, pH was neutralized by the
415 addition of 10% volume 1.0 M Tris-pH 8.0. The crude genomic extract was then used in PCR reactions
416 with primers flanking the targeted site. Amplicons were analyzed for insertions/deletions (indels) using a
417 TBE-PAGE gel. Indel sequence was determined by cloning amplicons into a TOPO-TA cloning vector
418 (Invitrogen) following the manufacturer's protocol. These cell lines were characterized in earlier work (29,
419 68), and modified here for luciferase expression by transducing cells with a lentiviral vector expressing
420 click beetle green luciferase (CBG)(69). We selected a population of cells stably expressing CBG based
421 on resistance to blasticidin expressed in the lentiviral vector as described previously.

422 MCF7 cells were purchased from the ATCC and verified cells by STR profiling through the
423 University of Michigan Advanced Genomics Core. We cultured MCF7 cells in DMEM medium with 10%
424 serum, 1% penicillin/streptomycin, and 1% glutamax (ThermoFisher Scientific) in an incubator set at 37°C
425 and 5% CO_2. We stably expressed click beetle green luciferase (CBG) in these cells by lentiviral
426 transduction as described previously(69). To stably express full-length, wild-type GIV in MCF7 and MDA-
427 MB-231-GIV KO cells, we used a Tol2 transposon system. The Tol2 transposon vector uses a CAG
428 promoter to drive constitutive expression of the cDNA for *CCDC88A* (the gene name for GIV) and a
429 hygromycin resistance gene linked by a P2A sequence (Vector Builder). We co-transfected cells with the
430 Tol2 GIV transposon and a Tol2 transposase (Vector Builder) at a 3:1 ratio of micrograms of plasmid
431 DNA using Fugene 6 (Promega) according to the manufacturer's directions. Control cells underwent
432 transfection with an empty Tol2 transposon and Tol2 transposase at the same ratio of plasmid DNA. Two
433 days after transfection, we added hygromycin (Sigma-Aldrich) to select batch populations of cells stably

434 expressing GIV. After obtaining stable cell lines, we did not culture resultant MCF7-GIV cells in
435 hygromycin. We stably expressed CBG in MCF7 cells as detailed for MDA-MB-231 cells.

436

437 **Immunoblotting**

438 To verify the expression of GIV in MCF7-GIV and MDA-MB-231-GIV KO/WT cells, equal aliquots of
439 whole-cell lysates (prepared using RIPA buffer) were loaded on a 8% SDS PAGE gel, and immunoblotting
440 was carried out for GIV with the mouse monoclonal antibody H-6 (Santa Cruz Biotechnology) as
441 described previously(70). Immunoblots were analyzed using a Gel Doc system (BioRad, Hercules, CA).

442

443 **RNA sequencing and identification of DEGs**

444 WT and GIV-KO MDA-MB231 cells grown in 0% and 10% serum concentration in p10 dishes (Corning)
445 for 16 h prior to harvest, and cell pellets were subsequently processed for RNA extraction using a kit
446 (R2052, Zymo Research) as per manufacturer's protocol. Isolated RNA has been processed for RNA
447 sequencing in the Illumina NovaSeq 6000 platform. Fastq sequence files have been mapped using the
448 human GRCh38 genome. Log normalized CPM expression files are submitted to GSE215822. A list of
449 DEGs is provided in **Supplemental Information 3**.

450

451 **Tandem Mass Tag™ (TMT) proteomics**

452 WT and GIV-KO MDA-MB231 cells were maintained in 0% and 10% serum concentration in p10 dishes
453 (Corning) for 16 h prior to harvest, and cell pellets were subsequently processed for TMT proteomics
454 using LUMOS Orbitrap-Fusion analyzer. Peptides are identified and mapped using Peaks X Pro pipeline.
455 Intensity ratio of each identified proteins in WT MDA-MB231 Vs GIV-KO MDA-MB231 cells has been
456 identified and selected if the significance score >20. The raw proteomics data has been submitted to
457 ProteomeXchange (PXD037253). A list of differentially expressed proteins is provided in **Supplemental**
458 **Information 4**.

459

460 **Soft agar growth assays**

461 We performed assays with minor modifications from a published protocol(71). Briefly, we made a base
462 layer of 0.7% agar (Sigma-Aldrich) dissolved in DMEM medium, adding 0.2% serum after the agar
463 solution cooled to ~37°C before transferring 1 ml per well to 6 well plates. After the base layer solidified
464 at room temperature, we prepared 0.35% low melting agar (Sigma) in DMEM medium, adding the same
465 concentration of serum as in the base layer and 5 x 10^4 cells per ml when the solution cooled to ~37°C

466 (n = 3 wells per cell type and serum condition). We immediately transferred 1 ml per well of the low
467 melting point agar/cell solution to each well and cooled the plate briefly at 4°C before placing in a cell
468 culture incubator. We added 0.5 ml fresh DMEM medium with 0.2% serum every 2 days. After one week,
469 we obtained 9 bright-field images per well on an inverted microscope (Olympus IX73 with 20X objective).
470 Immediately after microscopy, we added 150 µg/ml luciferin (Promega) to each well; incubated in a cell
471 culture incubator for 10 minutes; and then acquired a bioluminescence image of total viable cells on an
472 IVIS Lumina (30 second image, large field of view) (Perkin Elmer). A person blinded to experimental
473 conditions enumerated colonies and quantified imaging data (Living Image, Perkin Elmer).
474
475 **Cytotoxicity assays**
476 We performed cytotoxicity assays on MCF7 cells as described previously(72). Briefly, we seeded 7.5 x
477 10^3 MCF7 WT or MCF7-GIV cells per well in black wall 96 well plates (ThermoFisher Scientific, catalog
478 number 165305). One day after seeding in normal growth medium, we washed cells once with PBS and
479 then added various concentrations of drugs (tamoxifen, fulvenstrant, or 18albociclib; all purchased from
480 Tocris) in phenol red free DMEM (ThermoFisher Scientific) with 4 mM glucose, 1% serum, 1%
481 penicillin/streptomycin, 1% Glutamax, and 10 nM estrogen (n = 4 wells per cell type and concentration).
482 Three days later, we added 150 µg/ml luciferin per well; incubated in a cell culture incubator for 10
483 minutes; and then acquired a bioluminescence image of total viable cells on an IVIS Lumina (1 minute
484 image, large field of view). We quantified bioluminescence as radiance per well (LivingImage software)
485 and normalized data for each cell type and drug concentration to vehicle only.
486
487 **Animal studies**
488 The University of Michigan Institutional Care and Use of Animals Committee approved all animal
489 procedures. We used 8-10-week-old female NSG mice originally purchased from The Jackson
490 Laboratory and bred in the colony maintained by the University of Michigan Lab Animal Medicine
491 Program. Prior to mouse experiments, we cultured MDA-MB-231 WT and MDA-MB-231-GIV KO/WT
492 cells in serum-free DMEM with 25 mM glucose overnight. We verified that these cells did not lose viability
493 after overnight culture in serum-free medium relative to medium with 10% serum as determined by cell-
494 based measurements of CBG bioluminescence in an IVIS Lumina (Perkin Elmer). We injected 1 x 10^5
495 breast cancer cells per mouse (n = 5 per each cell type), verifying positioning of the 30g needle in the left
496 ventricle by return of pulsatile bright red blood as described(73). We imaged bioluminescence with an
497 IVIS Spectrum (Perkin Elmer) in mice at time points shown in the figure legend and quantified data with
498 Living Image software. For each mouse, we calculated the fold-change in bioluminescence relative to the

499 value obtained one day after injection to normalize for variations in injected amounts of cells. We
500 calculated area-under-the-curve ± SEM for total bioluminescence in each group.
501
502 **COMPUTATIONAL METHODS**

503 **Transcriptomic datasets**

504 All publicly available transcriptomic datasets were downloaded from National Center for Biotechnology
505 Information (NCBI) Gene Expression Omnibus website (GEO)(74-76) or European Molecular Biology
506 Laboratory (EMBL) European Bioinformatics Institute (EMBL-EBI) ArrayExpress website(77). All gene
507 expression datasets (**Supplementary Information 1**) were processed separately using the Hegemon
508 (hierarchical exploration of **gene** expression microarrays on-line) data analysis framework (78-80). We
509 did not combine datasets that belong to two different platforms. See **Supplemental Information 1** for
510 the degree of heterogeneity among samples in the datasets used in this work.

511

512 ***StepMiner* analysis**

513 *StepMiner* is an algorithm that identifies step-wise transitions using step function in a time-series
514 data(81). *StepMiner* undergoes an adaptive regression scheme to verify the best possible up and down
515 steps based on sum-of-square errors. The steps are placed between time points at the sharpest change
516 between expression levels, which gives us the information about timing of the gene expression-switching
517 event. To fit a step function, the algorithm evaluates all possible steps for each position and computes
518 the average of the values on both sides of a step for the constant segments. An adaptive regression
519 scheme is used that chooses the step positions that minimize the square error with the fitted data. Finally,
520 a regression test statistic is computed as follows:

521 $$F\ stat = \frac{\sum_{i=1}^{n}(\widehat{X}_i - \bar{X})^2/(m-1)}{\sum_{i=1}^{n}(X_i - \widehat{X}_i)^2/(n-m)}$$

522 Where X_i for $i = 1$ to n are the values, $\widehat{X}_i$ for $i = 1$ to n are fitted values. M is the degrees of freedom
523 used for the adaptive regression analysis. $\bar{X}$ is the average of all the values: $\bar{X} = \frac{1}{n} * \sum_{j=1}^{n} X_j$. For a step
524 position at k, the fitted values $\widehat{X}_l$ are computed by using $\frac{1}{k} * \sum_{j=1}^{n} X_j$ for $i = 1$ to k and $\frac{1}{(n-k)} * \sum_{j=k+1}^{n} X_j$
525 for $i = k + 1$ to n.

526

527 **Composite gene signature analysis using Boolean Network Explorer (BoNE)**

528 Boolean network explorer (BoNE) provides an integrated platform for the construction, visualization and
529 querying of a gene expression signature underlying a disease or a biological process in three steps: First,
530 the expression levels of all genes in these datasets were converted to binary values (high or low) using
531 the StepMiner algorithm. Second, Gene expression values were normalized according to a modified Z-
532 score approach centered around *StepMiner* threshold (formula = (expr – SThr)/3*stddev). Third, the
533 normalized expression values for every genes were added together to create the final score for the gene
534 signature. The samples were ordered based on the final signature score. Classification of sample
535 categories using this ordering is measured by ROC-AUC (Receiver Operating Characteristics Area Under
536 The Curve) values. Welch's Two Sample t-test (unpaired, unequal variance (equal_var=False), and
537 unequal sample size) parameters were used to compare the differential signature score in different
538 sample categories. Violin, Swarm and Bubble plots are created using python seaborn package version
539 0.10.1. Pathway enrichment analyses for genes were carried out via the reactome database and
540 algorithm(82). Violin, Swarm and Bubble plots are created using python seaborn package version 0.10.1.
541 A list of all gene signatures used in this work is provided in **Supplemental Information 2**.

542

543 **Survival outcome analyses**

544 Kaplan-Meier (KM) analyses were done for different gene signatures. The high and low groups were
545 separated based on *StepMiner* threshold on the composite score of the gene expression values. The
546 statistical significance of KM plots was assessed by log rank test. Kaplan-Meier analyses were performed
547 using lifelines python package version 0.14.6.

548

549

550 **Protein-protein interaction network construction and analysis**

551 Upregulated proteins in WT MDA-MB-231 cells in comparison with the GIV-KO MDA-MB-231 cells are
552 identified with an intensity ratio cutoff of >=2 and with a significance value >= 20. Interaction edges
553 between the identified proteins are fetched from the STRING human interactome database and
554 represented in Figure 4g as a protein-protein interaction network (PPIN) using Gephi 9.02. Degree
555 distribution of the PPIN computed using python network package.

556

557 ## STATISTICAL ANALYSIS

558 Gene signature is used to classify sample categories and the performance of the multi- class classification
559 is measured by ROC-AUC (Receiver Operating Characteristics Area Under the Curve) values. A color-

560 coded bar plot is combined with a density plot to visualize the gene signature-based classification. All
561 statistical tests were performed using R version 3.2.3 (2015-12-10). Standard t-tests were performed
562 using python scipy.stats.ttest_ind package (version 0.19.0) with Welch's Two Sample t-test
563 (unpaired, unequal variance (equal_var=False), and unequal sample size) parameters. Multiple
564 hypothesis correction was performed by adjusting *p* values with statsmodels.stats.multitest.multipletests
565 (fdr_bh: Benjamini/Hochberg principles). Sample number of each analysis is provided with associated
566 plots beside each GSE ID no. or sample name. The statistical significance of KM plots was assessed by
567 log rank test. Pathway enrichment analyses of gene lists were carried out using the Reactome
568 database(83) (http://reactome.org) and the Cytoscape plug-in, CluGo
569 (http://www.ici.upmc.fr/cluego/cluegoDownload.shtml).

570

571

Acknowledgments

We thank Debashis Sahoo (UC San Diego, Boolean Lab) for access to computational resources. This work was supported by the United States National Institutes of Health grants, CA100768, AI141630, CA160911 and CA238042 (to PG), CA238042, CA210152, CA238023, CA225549, CA221807, and CA222563 (to GDL); and CA221807 (KEL). GDL and KEL acknowledge funding from the W.M. Keck Foundation.

Competing Interest Statement: The authors declare no competing interests other than a filed patent on methodology and utility of the gene signature in the clinical setting.

Author Contributions: S.S carried out all the computational analyses in this work. A.F., P.G and G.D.L designed, carried out and analyzed all experiments. S.S and P.G created all the figures. K.E.L. provided new reagents. B.P and K.Y guided S.S and P.G in data analysis and interpretation. S.S and G.D.L wrote methods, and all authors edited the manuscript. P.G and G.D.L conceptualized, designed, and supervised the project. P.G, S.S, G.D.L wrote the manuscript, and all authors edited and approved the same.

589 **References**

590 1. A. W. Lambert, D. R. Pattabiraman, R. A. Weinberg, Emerging Biological Principles of Metastasis. *Cell*
591 **168**, 670-691 (2017).
592 2. C. L. Chaffer, R. A. Weinberg, A perspective on cancer cell metastasis. *Science* **331**, 1559-1564 (2011).
593 3. S. A. Joosse, T. M. Gorges, K. Pantel, Biology, detection, and clinical implications of circulating tumor
594 cells. *EMBO Mol Med* **7**, 1-11 (2015).
595 4. Z. Ju *et al.*, Telomere dysfunction induces environmental alterations limiting hematopoietic stem cell
596 function and engraftment. *Nat Med* **13**, 742-747 (2007).
597 5. S. Ju *et al.*, Detection of circulating tumor cells: opportunities and challenges. *Biomark Res* **10**, 58 (2022).
598 6. M. B. Amin *et al.*, The Eighth Edition AJCC Cancer Staging Manual: Continuing to build a bridge from a
599 population-based to a more "personalized" approach to cancer staging. *CA Cancer J Clin* **67**, 93-99
600 (2017).
601 7. R. Y. Ebright *et al.*, Deregulation of ribosomal protein expression and translation promotes breast cancer
602 metastasis. *Science* **367**, 1468-1473 (2020).
603 8. B. M. Szczerba *et al.*, Neutrophils escort circulating tumour cells to enable cell cycle progression. *Nature*
604 **566**, 553-557 (2019).
605 9. M. Bulfoni *et al.*, In patients with metastatic breast cancer the identification of circulating tumor cells in
606 epithelial-to-mesenchymal transition is associated with a poor prognosis. *Breast Cancer Res* **18**, 30
607 (2016).
608 10. M. Yu *et al.*, Circulating breast tumor cells exhibit dynamic changes in epithelial and mesenchymal
609 composition. *Science* **339**, 580-584 (2013).
610 11. S. Wu *et al.*, Classification of circulating tumor cells by epithelial-mesenchymal transition markers. *PLoS*
611 *One* **10**, e0123976 (2015).
612 12. X. Liu *et al.*, Epithelial-type systemic breast carcinoma cells with a restricted mesenchymal transition are
613 a major source of metastasis. *Sci Adv* **5**, eaav4275 (2019).
614 13. H. Thangavel *et al.*, A CTC-Cluster-Specific Signature Derived from OMICS Analysis of Patient-Derived
615 Xenograft Tumors Predicts Outcomes in Basal-Like Breast Cancer. *J Clin Med* **8** (2019).
616 14. E. Schuster *et al.*, Better together: circulating tumor cell clustering in metastatic cancer. *Trends Cancer* **7**,
617 1020-1032 (2021).
618 15. N. Aceto *et al.*, Circulating tumor cell clusters are oligoclonal precursors of breast cancer metastasis. *Cell*
619 **158**, 1110-1122 (2014).
620 16. R. Taftaf *et al.*, ICAM1 initiates CTC cluster formation and trans-endothelial migration in lung metastasis
621 of breast cancer. *Nat Commun* **12**, 4867 (2021).
622 17. A. M. Dujon *et al.*, Is There. *Cancers (Basel)* **13** (2021).
623 18. C. Donato *et al.*, Hypoxia Triggers the Intravasation of Clustered Circulating Tumor Cells. *Cell Rep* **32**,
624 108105 (2020).
625 19. Z. Diamantopoulou *et al.*, The metastatic spread of breast cancer accelerates during sleep. *Nature* **607**,
626 156-162 (2022).
627 20. I. Pinilla-Macua, A. Grassart, U. Duvvuri, S. C. Watkins, A. Sorkin, EGF receptor signaling,
628 phosphorylation, ubiquitylation and endocytosis in tumors in vivo. *Elife* **6** (2017).
629 21. K. Witzeneder *et al.*, Human-derived alternatives to fetal bovine serum in cell culture. *Transfus Med*
630 *Hemother* **40**, 417-423 (2013).
631 22. Y. Oka, D. N. Orth, Human plasma epidermal growth factor/beta-urogastrone is associated with blood
632 platelets. *J Clin Invest* **72**, 249-259 (1983).
633 23. A. P. Savage, V. K. Chatterjee, H. Gregory, S. R. Bloom, Epidermal growth factor in blood. *Regul Pept* **16**,
634 199-206 (1986).

24. C. Callegari *et al.*, The source of urinary epidermal growth factor in humans. *Eur J Appl Physiol Occup Physiol* **58**, 26-31 (1988).
25. I. Baccelli *et al.*, Identification of a population of blood circulating tumor cells from breast cancer patients that initiates metastasis in a xenograft assay. *Nat Biotechnol* **31**, 539-544 (2013).
26. D. Hanahan, R. A. Weinberg, Hallmarks of cancer: the next generation. *Cell* **144**, 646-674 (2011).
27. S. A. Aaronson, Growth factors and cancer. *Science* **254**, 1146-1153 (1991).
28. M. Chigira, K. Noda, H. Watanabe, Autonomy in tumor cell proliferation. *Med Hypotheses* **32**, 249-254 (1990).
29. L. Qiao *et al.*, A circuit for secretion-coupled cellular autonomy in multicellular eukaryotic cells. *Mol Syst Biol*, e11127 (2023).
30. I. C. Lo *et al.*, Activation of Gαi at the Golgi by GIV/Girdin imposes finiteness in Arf1 signaling. *Dev Cell* **33**, 189-203 (2015).
31. L. Qiao, P. Ghosh, P. Rangamani, Design principles of improving the dose-response alignment in coupled GTPase switches. *NPJ Syst Biol Appl* **9**, 3 (2023).
32. K. Liu *et al.*, Evaluating cell lines as models for metastatic breast cancer through integrative analysis of genomic data. *Nat Commun* **10**, 2138 (2019).
33. P. Ghosh, Heterotrimeric G proteins as emerging targets for network based therapy in cancer: End of a long futile campaign striking heads of a Hydra. *Aging (Albany NY)* **7**, 469-474 (2015).
34. K. Takahashi, S. Yamanaka, Induction of pluripotent stem cells from mouse embryonic and adult fibroblast cultures by defined factors. *Cell* **126**, 663-676 (2006).
35. T. M. Malta *et al.*, Machine Learning Identifies Stemness Features Associated with Oncogenic Dedifferentiation. *Cell* **173**, 338-354.e315 (2018).
36. J. Yang *et al.*, Guidelines and definitions for research on epithelial-mesenchymal transition. *Nat Rev Mol Cell Biol* **21**, 341-352 (2020).
37. M. S. Brown *et al.*, Phenotypic heterogeneity driven by plasticity of the intermediate EMT state governs disease progression and metastasis in breast cancer. *Sci Adv* **8**, eabj8002 (2022).
38. Y. C. Chen *et al.*, Functional Isolation of Tumor-Initiating Cells using Microfluidic-Based Migration Identifies Phosphatidylserine Decarboxylase as a Key Regulator. *Sci Rep* **8**, 244 (2018).
39. D. P. Cook, B. C. Vanderhyden, Transcriptional census of epithelial-mesenchymal plasticity in cancer. *Sci Adv* **8**, eabi7640 (2022).
40. M. C. Guadamillas, A. Cerezo, M. A. Del Pozo, Overcoming anoikis--pathways to anchorage-independent growth in cancer. *J Cell Sci* **124**, 3189-3197 (2011).
41. X. Zhu *et al.*, In vivo flow cytometry reveals a circadian rhythm of circulating tumor cells. *Light Sci Appl* **10**, 110 (2021).
42. E. Ozkumur *et al.*, Inertial focusing for tumor antigen-dependent and -independent sorting of rare circulating tumor cells. *Sci Transl Med* **5**, 179ra147 (2013).
43. A. Shinde *et al.*, Spleen Tyrosine Kinase-Mediated Autophagy Is Required for Epithelial-Mesenchymal Plasticity and Metastasis in Breast Cancer. *Cancer Res* **79**, 1831-1843 (2019).
44. S. Khoshbakht, S. Azimzadeh Jamalkandi, A. Masudi-Nejad, Involvement of immune system and Epithelial-Mesenchymal-Transition in increased invasiveness of clustered circulatory tumor cells in breast cancer. *BMC Med Genomics* **14**, 273 (2021).
45. M. P. Ward *et al.*, Platelets, immune cells and the coagulation cascade; friend or foe of the circulating tumour cell? *Mol Cancer* **20**, 59 (2021).
46. P. Aouad *et al.*, Epithelial-mesenchymal plasticity determines estrogen receptor positive breast cancer dormancy and epithelial reconversion drives recurrence. *Nat Commun* **13**, 4975 (2022).
47. P. Balcik-Ercin, L. Cayrefourcq, R. Soundararajan, S. A. Mani, C. Alix-Panabières, Epithelial-to-Mesenchymal Plasticity in Circulating Tumor Cell Lines Sequentially Derived from a Patient with Colorectal Cancer. *Cancers (Basel)* **13** (2021).

683 48. K. J. Cheung *et al.*, Polyclonal breast cancer metastases arise from collective dissemination of keratin 14-
684 expressing tumor cell clusters. *Proc Natl Acad Sci U S A* **113**, E854-863 (2016).
685 49. R. D. Z. Mullins, A. Pal, T. F. Barrett, M. E. Heft Neal, S. V. Puram, Epithelial-Mesenchymal Plasticity in
686 Tumor Immune Evasion. *Cancer Res* **82**, 2329-2343 (2022).
687 50. P. Chakraborty *et al.*, Analysis of immune subtypes across the epithelial-mesenchymal plasticity
688 spectrum. *Comput Struct Biotechnol J* **19**, 3842-3851 (2021).
689 51. A. Dongre, R. A. Weinberg, New insights into the mechanisms of epithelial-mesenchymal transition and
690 implications for cancer. *Nat Rev Mol Cell Biol* **20**, 69-84 (2019).
691 52. M. Dhar *et al.*, Functional profiling of circulating tumor cells with an integrated vortex capture and
692 single-cell protease activity assay. *Proc Natl Acad Sci U S A* **115**, 9986-9991 (2018).
693 53. S. Ghannoum *et al.*, DIscBIO: A User-Friendly Pipeline for Biomarker Discovery in Single-Cell
694 Transcriptomics. *Int J Mol Sci* **22** (2021).
695 54. T. S. Fedi P, Aaronson SA, *Cancer Medicine*. B. R. C. Holland J.F, Morton D.L, Frei E, Kufe D.W and
696 Weichselbaum R.R, Ed., Growth factors (Williams and Wilkins, Baltimor, MD, 1997).
697 55. P. A. Martínez-Carpio *et al.*, Secretion and dual regulation between epidermal growth factor and
698 transforming growth factor-beta1 in MDA-MB-231 cell line in 42-hour-long cultures. *Cancer Lett* **147**, 25-
699 29 (1999).
700 56. P. Wee, Z. Wang, Epidermal Growth Factor Receptor Cell Proliferation Signaling Pathways. *Cancers*
701 *(Basel)* **9** (2017).
702 57. D. C. Voon *et al.*, EMT-induced stemness and tumorigenicity are fueled by the EGFR/Ras pathway. *PLoS*
703 *One* **8**, e70427 (2013).
704 58. A. A. Changavi, A. Shashikala, A. S. Ramji, Epidermal Growth Factor Receptor Expression in Triple
705 Negative and Nontriple Negative Breast Carcinomas. *J Lab Physicians* **7**, 79-83 (2015).
706 59. I. M. Kjær *et al.*, Dysregulated EGFR pathway in serum in early-stage breast cancer patients: A case
707 control study. *Sci Rep* **10**, 6714 (2020).
708 60. F. J. Esteva *et al.*, Clinical utility of serum HER2/neu in monitoring and prediction of progression-free
709 survival in metastatic breast cancer patients treated with trastuzumab-based therapies. *Breast Cancer*
710 *Res* **7**, R436-443 (2005).
711 61. R. E. Payne *et al.*, Measurements of EGFR expression on circulating tumor cells are reproducible over
712 time in metastatic breast cancer patients. *Pharmacogenomics* **10**, 51-57 (2009).
713 62. G. Kallergi *et al.*, Phosphorylated EGFR and PI3K/Akt signaling kinases are expressed in circulating tumor
714 cells of breast cancer patients. *Breast Cancer Res* **10**, R80 (2008).
715 63. X. Liu *et al.*, EGFR inhibition blocks cancer stem cell clustering and lung metastasis of triple negative
716 breast cancer. *Theranostics* **11**, 6632-6643 (2021).
717 64. L. Brüser, S. Bogdan, Adherens Junctions on the Move-Membrane Trafficking of E-Cadherin. *Cold Spring*
718 *Harb Perspect Biol* **9** (2017).
719 65. R. B. Hazan, L. Norton, The epidermal growth factor receptor modulates the interaction of E-cadherin
720 with the actin cytoskeleton. *J Biol Chem* **273**, 9078-9084 (1998).
721 66. T. T. Kwan *et al.*, A Digital RNA Signature of Circulating Tumor Cells Predicting Early Therapeutic
722 Response in Localized and Metastatic Breast Cancer. *Cancer Discov* **8**, 1286-1299 (2018).
723 67. N. S. Amer Ali Abd El-Hafeez , Anirban Chakraborty , Jason Ear , Suchismita Roy , Pranavi
724 Chamarthi , Navin Rajapakse , Soumita Das , Kathryn E. Luker , Tapas K. Hazra , Gary D.
725 Luker , Pradipta Ghosh (2021) Regulation of DNA damage response by trimeric G-protein Signaling.
726 68. A. A. Abd El-Hafeez *et al.*, Regulation of DNA damage response by trimeric G-proteins. *iScience* **26**,
727 105973 (2023).
728 69. S. P. Cavnar *et al.*, Modeling selective elimination of quiescent cancer cells from bone marrow.
729 *Neoplasia* **17**, 625-633 (2015).

730 70. M. C. Smith *et al.*, CXCR4 regulates growth of both primary and metastatic breast cancer. *Cancer Res* **64**,
731 8604-8612 (2004).
732 71. S. Borowicz *et al.*, The soft agar colony formation assay. *J Vis Exp*, e51998 (2014).
733 72. J. M. Buschhaus *et al.*, Effects of iron modulation on mesenchymal stem cell-induced drug resistance in
734 estrogen receptor-positive breast cancer. *Oncogene* **41**, 3705-3718 (2022).
735 73. A. C. Stacer *et al.*, Endothelial CXCR7 regulates breast cancer metastasis. *Oncogene* **35**, 1716-1724
736 (2016).
737 74. R. Edgar, M. Domrachev, A. E. Lash, Gene Expression Omnibus: NCBI gene expression and hybridization
738 array data repository. *Nucleic Acids Res* **30**, 207-210 (2002).
739 75. T. Barrett *et al.*, NCBI GEO: archive for functional genomics data sets--update. *Nucleic Acids Res* **41**,
740 D991-995 (2013).
741 76. T. Barrett *et al.*, NCBI GEO: mining tens of millions of expression profiles--database and tools update.
742 *Nucleic Acids Res* **35**, D760-765 (2007).
743 77. L. A. Peters *et al.*, A functional genomics predictive network model identifies regulators of inflammatory
744 bowel disease. *Nat Genet* **49**, 1437-1449 (2017).
745 78. P. Dalerba *et al.*, Single-cell dissection of transcriptional heterogeneity in human colon tumors. *Nat*
746 *Biotechnol* **29**, 1120-1127 (2011).
747 79. P. Dalerba *et al.*, CDX2 as a Prognostic Biomarker in Stage II and Stage III Colon Cancer. *N Engl J Med*
748 **374**, 211-222 (2016).
749 80. J. P. Volkmer *et al.*, Three differentiation states risk-stratify bladder cancer into distinct subtypes. *Proc*
750 *Natl Acad Sci U S A* **109**, 2078-2083 (2012).
751 81. D. Sahoo, D. L. Dill, R. Tibshirani, S. K. Plevritis, Extracting binary signals from microarray time-course
752 data. *Nucleic Acids Res* **35**, 3705-3712 (2007).
753 82. A. Fabregat *et al.*, The Reactome Pathway Knowledgebase. *Nucleic Acids Res* **46**, D649-D655 (2018).
754 83. B. Jassal *et al.*, The reactome pathway knowledgebase. *Nucleic Acids Res* **48**, D498-D503 (2020).

755

756

757

Legends for Figures and Tables

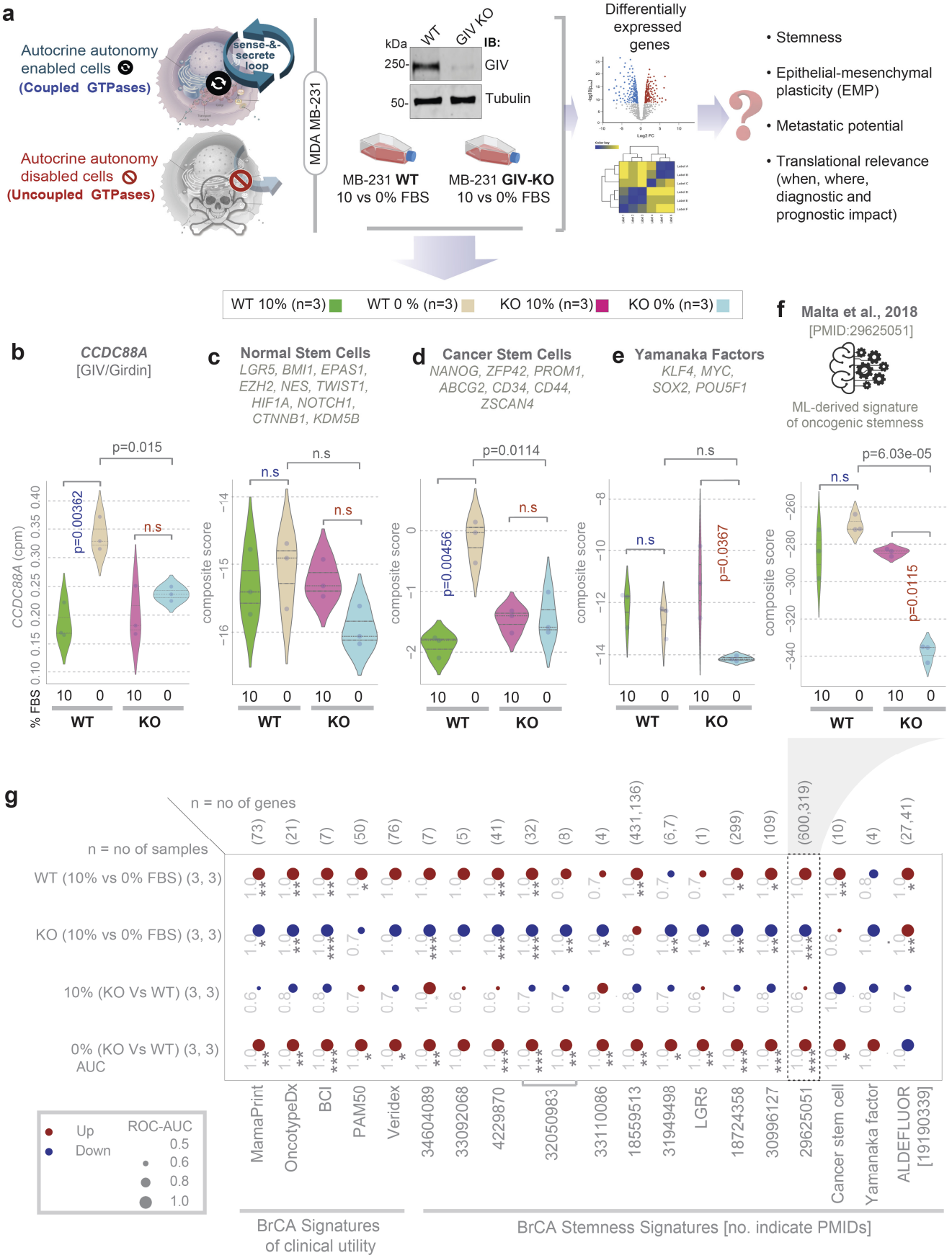

Figure 1. **Growth signaling autonomy is required for the induction or maintenance of stemness**

761 **a.** Schematic displays study design. Autocrine autonomy-endowed cells are compared against cells in which
762 such autonomy is disabled (autonomy-impaired) by depletion of GIV (GIV-KO). Cells are grown in the presence
763 or absence of exogenous growth factors (0% FBS) to study the biological and translational relevance of autocrine
764 autonomy in breast cancers.

765 **b-f.** Violin plots display the single (b) or composite (c-f) score of selected gene signatures. P values based on
766 Welch's T-test, comparing 10% vs 0% growth conditions in WT (blue) and KO (red) cells. Blue and red font for
767 p values indicate, significant up- or downregulation, respectively.

768 **g.** Expression of various stemness-associated gene signatures and clinically used breast cancer gene
769 signatures, in parental (WT) vs GIV-KO (KO, by CRISPR) MDA MB231 cells grown in 10% or 0% FBS is
770 visualized as bubble plots of ROC-AUC values (radius of circles are based on the ROC-AUC) demonstrating the
771 direction of gene regulation (Up, red; Down, blue) for the classification of WT and KO samples in 10% and 0%
772 FBS conditions based on the indicated gene signatures (bottom). BCI, breast cancer index. Nos. indicate PMIDs.

773 *Statistics*: *p* values based on Welch's T-test (of composite score of gene expression values) are provided either
774 as exact values (in panels b-f) or using standard code in panel g (''p>0.1, '.'p<=0.1, *p<=0.05, **p<=0.01,
775 ***p<=0.001) next to the ROC-AUC.

776 n.s., not significant. See **Figure S1** for violin plots of representative signatures.

777

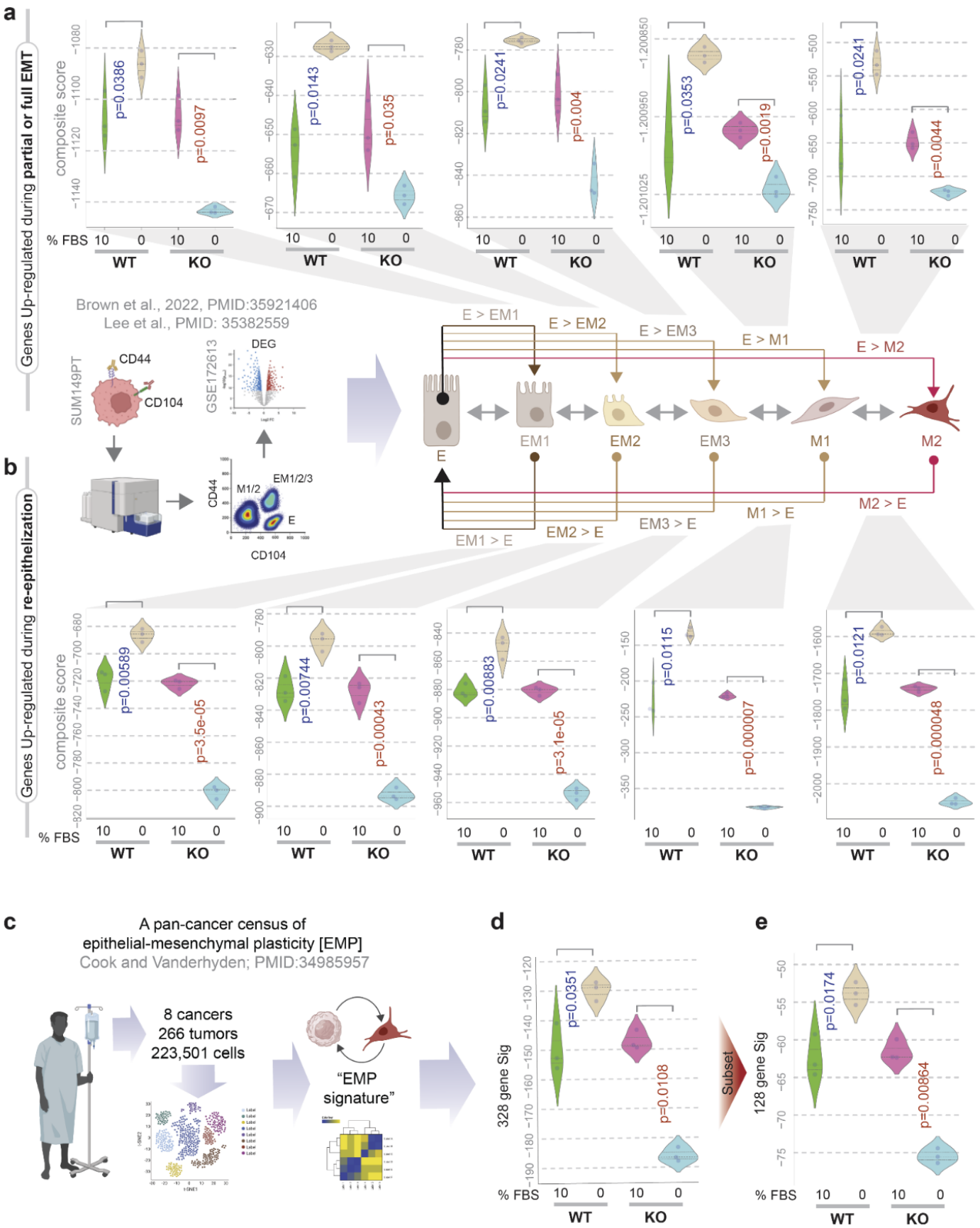

Figure 2. Growth signaling autonomy is required for the induction of molecular programs for EMT, re-epithelization and epithelial-mesenchymal plasticity (EMP)

781 **a.** Violin plots display the composite score of various gene signatures in parental (WT) and GIV-depleted (GIV-
782 KO) MDA MB-231 cells, which are induced during epithelial cell transition into partial (EM1, EM2, EM3) or full
783 (M1 and M2) EMT states.

784 **b.** Violin plots display the composite score of various gene signatures in parental (WT) and GIV-depleted (GIV-
785 KO) MDA MB-231 cells, which are induced during the re-epithelization of partial (EM1, EM2, EM3) or full (M1
786 and M2) EMT states.

787 **c-e**. Schematic (c) summarizes the study design that resulted in the discovery of the pan-cancer transcriptional
788 census of epithelial mesenchymal plasticity (EMP) derived by single cell seq (39). Violin plots (d-e) display the
789 composite score of the EMP signature in parental (WT) and GIV-depleted (GIV-KO) MDA MB-231 cells. Panel
790 d shows the expression profile of all 328 genes in the EMP signature, representing various cells in the tumor
791 microenvironment. Panel e shows the expression profile of a subset of 128 genes in the EMP signature that is
792 specifically enriched in cancer cells.

793 *p* values based on Welch's T-test, comparing 10% vs 0% growth conditions in WT (blue) and KO (red) cells.
794 Blue and red font for p values indicate, significant up- or downregulation, respectively. See **Figure S2** for other
795 gene signatures for EMT, CTC clusters and MET.

796

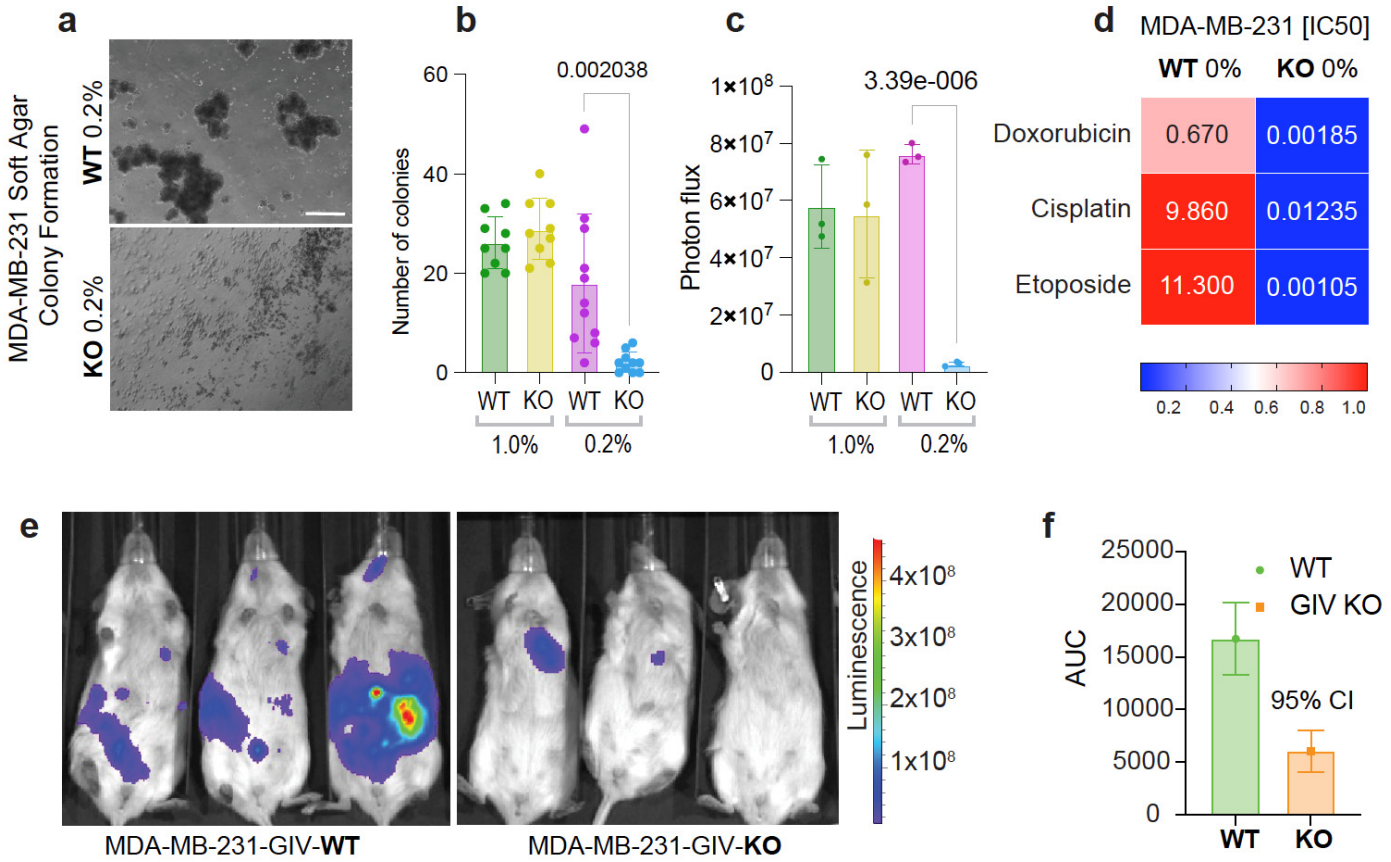

Figure 3. GIV-dependent autonomy is required for growth in growth factor-restricted conditions, resilience to chemotherapeutics and metastatic seeding.

a-c. Images (a) display representative fields acquired by light microscopy from soft-agar colony growth assays (see Methods) on luciferase-expressing parental (WT) and GIV-KO MDA-MB-231 cells, conducted in serum-restricted conditions. Scale bar = 30 µm. Bar plots (b) display the number of colonies/high-power field (HPF) of parental (WT) and GIV-KO MDA-MB-231 cells, quantified using images in 1% and 0.2% FBS (0% FBS for 1 week prevents colony formation altogether). Bar graphs (c) display the average photon flux emitted from colonies in above explained experimental setup. Results in b-c are representative of 3 biological repeats, and 20-40 HPFs were quantified in each repeat. Error bars in c represent S.E.M. p values were calculated by two-tailed t-test.

d. IC50 values for three commonly used chemotheraputic drugs, displayed as a heatmap.

e-f. Representative whole mouse bioluminescence images (e) of mice acquired on day #22 after intracardiac injection of serum-deprived parental (WT) and GIV-KO MDA-MB-231 cells in panel a. The logarithmic pseudo-color scale depicts the range of bioluminescence values with red being the highest and blue the lowest. Bar graphs (f) display mean values ± S.E.M. for area-under-the-curve (AUC) for total bioluminescence from days 1-29 after intracardiac injection for each group. N = 5 mice per condition.

See also **Figure S3** for similar studies on MCF7 cells (that lack endogenous GIV).

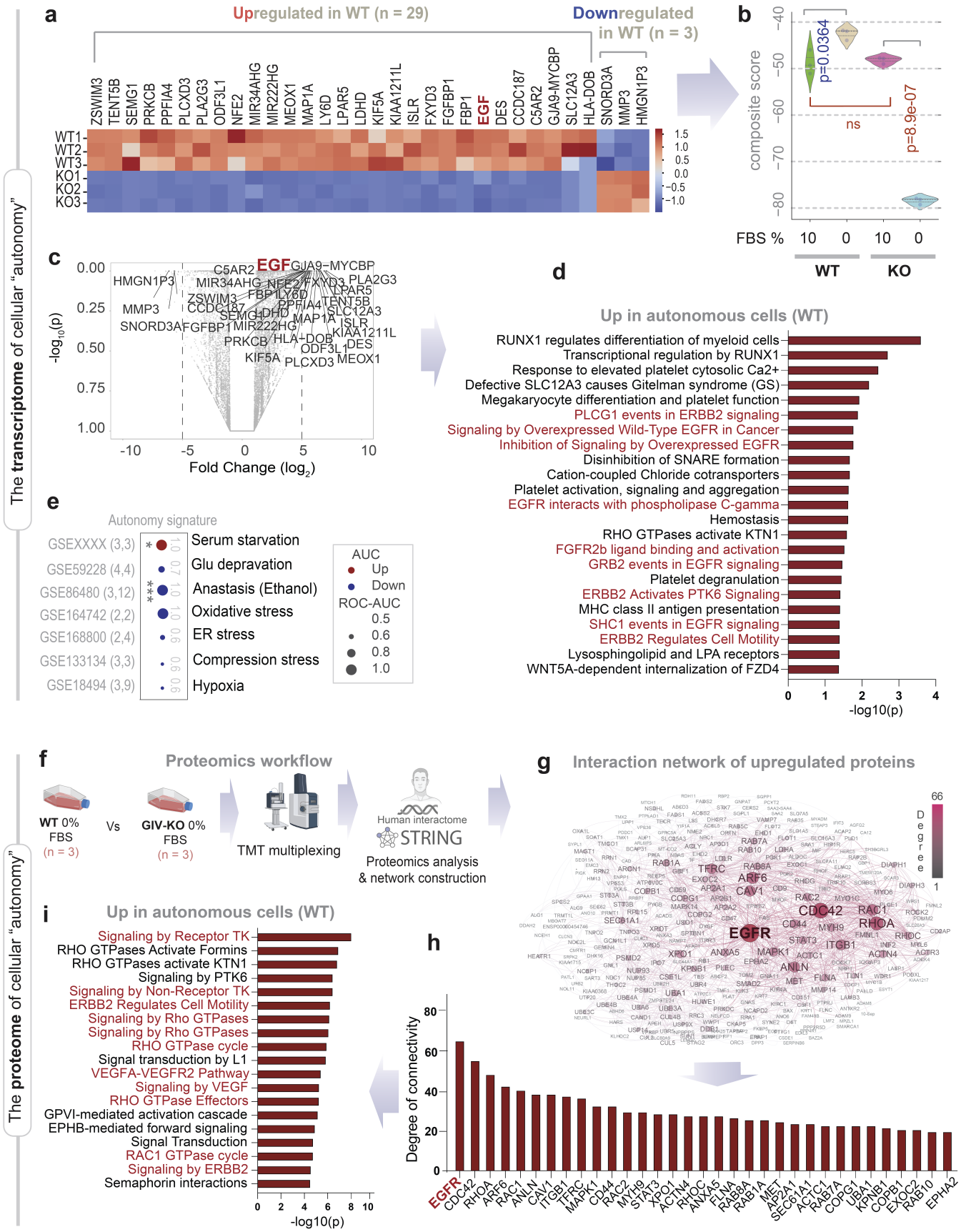

Figure 4. Genes and proteins differentially expressed between autonomy-endowed (WT) and -impaired (GIV-KO) MDA-MB-231 cells.

818 **a.** Heatmap displays DEGs (29 up- and 3 down-regulated; LogFC >5, pAdj <0.01) in MDA MB-231 parental (WT)
819 cells compared to its GIV-depleted (KO by CRISPR) counterparts grown in 0% FBS for 16 h.

820 **b**. Violin plots display the composite score of the DEGs in a (used as an 'autonomy signature') in parental (WT)
821 and GIV-depleted (GIV-KO) MDA MB-231 cells.

822 **c**. Volcano plot of the differentially expressed genes between WT and GIV-KO MDA MB-321 cells.

823 **d.** Reactome pathway analyses of the pathways enriched in the genes upregulated in WT vs KO MDA MB-231
824 cells. Red, pathways associated with EGFR/ERBB signaling. See also **Figure S4** for the Reactome pathway for
825 the genes down-regulated in autonomy-endowed (WT) cells.

826 **e**. Expression of autonomy signature in cells subjected to various stressors is visualized as bubble plots of ROC-
827 AUC values (radius of circles are based on the ROC-AUC) demonstrating the direction of gene regulation (Up,
828 red; Down, blue) for the classification of control vs stress conditions. MDA MB-231 cells were used in all except
829 anastasis, which was done in HeLa cells. *p* values based on Welch's T-test (of composite score of gene
830 expression values) are provided either as exact values or using standard code (''p>0.1, '.'p<=0.1, *p<=0.05,
831 **p<=0.01, ***p<=0.001) next to the ROC-AUC. See **Figure S5a-j** for visualization of the data as violin plots.

832 **f-h**. Schematic (f) of the workflow for proteomic analyses. Briefly, differentially expressed proteins (upregulated
833 in WT, compared to KO; n = 3 samples each), as determined by TMT proteomics were used for protein-protein
834 network construction using the human interactome database curated by STRING (Search Tool for the Retrieval
835 of Interacting Genes/Proteins; https://string-db.org/). The resultant network of protein-protein interaction is
836 displayed in g. Node size indicates the degree of connectivity within the network. Degree of connectivity of nodes
837 with a z score of degree (Z_d) >=1 is represented as a bar plot in h.

838 i. Reactome pathway analyses of the most connected nodes (Z_d >= 3) that are upregulated in WT vs KO MDA
839 MB-231 cells. Red, pathways associated with EGFR/ERBB signaling.

840

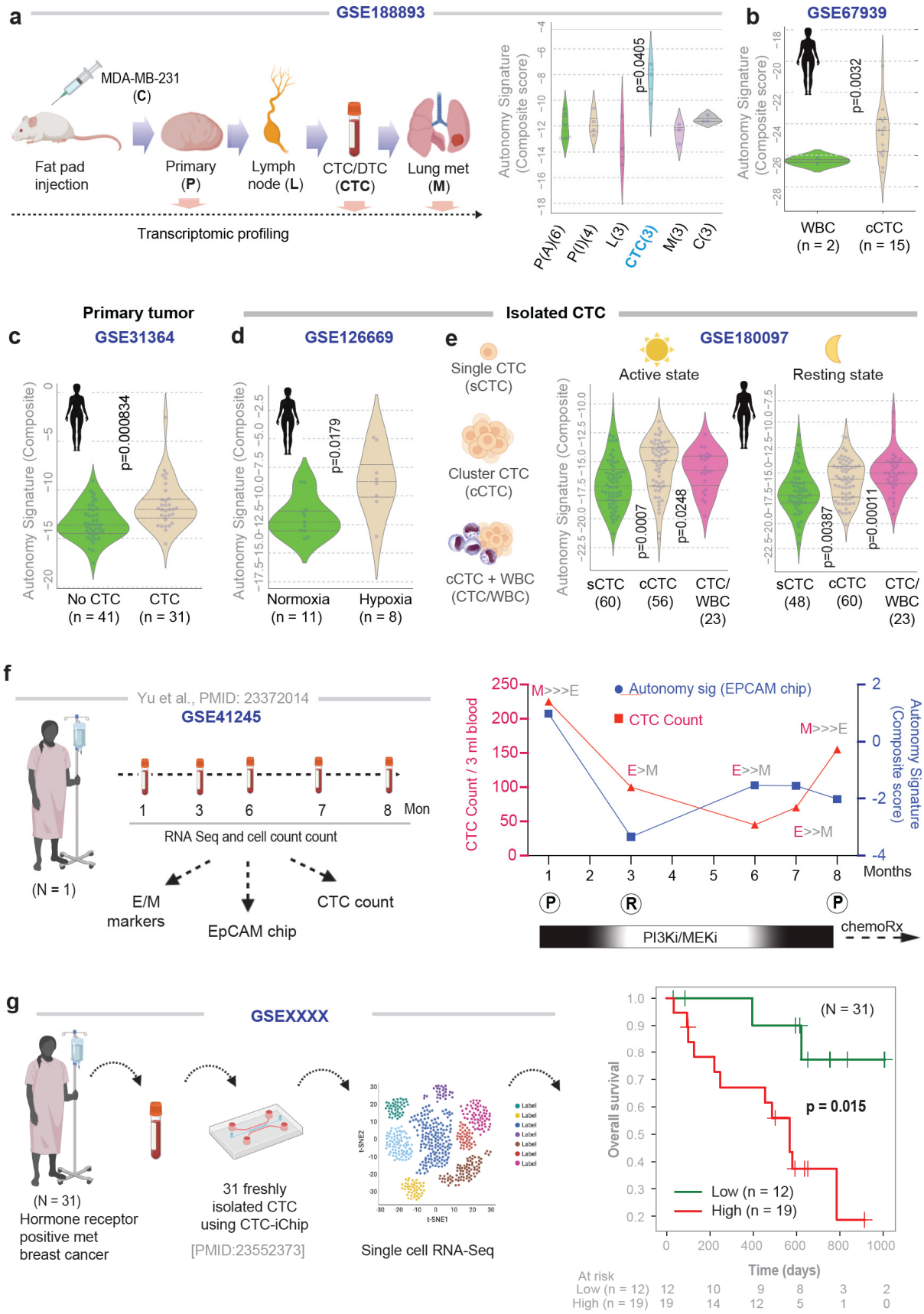

Figure 5. Autonomy signature is induced in CTCs, tracks treatment response and carries poor prognosis.

844 **a.** *Left:* Schematic displays of the study design for a publicly available dataset, GSE103639, in which the MDA
845 MB-231 breast cancer cell line was injected into NOD scid female mice and then RNA seq was carried out for
846 primary tumors from both axillary (P-A) and inguinal (P-I) locations, lymph nodes (L), isolated CTCs, and
847 metastases to the lung (M). *Right:* Violin plots display the composite score for autonomy signature in all
848 samples and assessed for statistically significant differences compared to the primary tumor by Welch's t-test.

849 **b-e**. Violin plots display the composite score for autonomy signature in various human datasets comparing 15
850 CTC clusters from a single patient during one blood draw against WBC control (b), primary tumors with/without
851 detectable CTCs (c), CTCs challenged or not with hypoxia (d) and single vs. clustered CTCs collected during
852 different times of the day (e). Statistical significance was assessed Welch's t-test.

853 **f**. *Left*: Schematic displays study design used in a publicly available dataset, GSE41245. *Right*: Graph tracks the
854 abundance of CTCs (CTC count; blue, left y axis), overlaid on composite score of the levels of expression of
855 genes in the autonomy signature in CTCs (EpCAM chip; red, right y axis). The ratio of epithelial (E) vs
856 mesenchymal (M) markers, as determined by qPCR and reported in the original study by RTqPCR on a panel
857 of markers is indicated. X-axis (time) is annotated with the therapeutic regimen and clinically determined disease
858 status; (P) progression, and (R), response.

859 **g.** *Left:* Schematic showing the study design in which CTCs were isolated from 31 unique subjects with MBC
860 using CTC-iChip microfluidic device and underwent single-cell CTC RNA-seq (GSE215886). *Right:* KM curves
861 of overall survival on the same cohort, stratified based on high (red) vs low (green) autonomy signature.
862 Statistical significance (p value) was determined by the log-rank test.

863

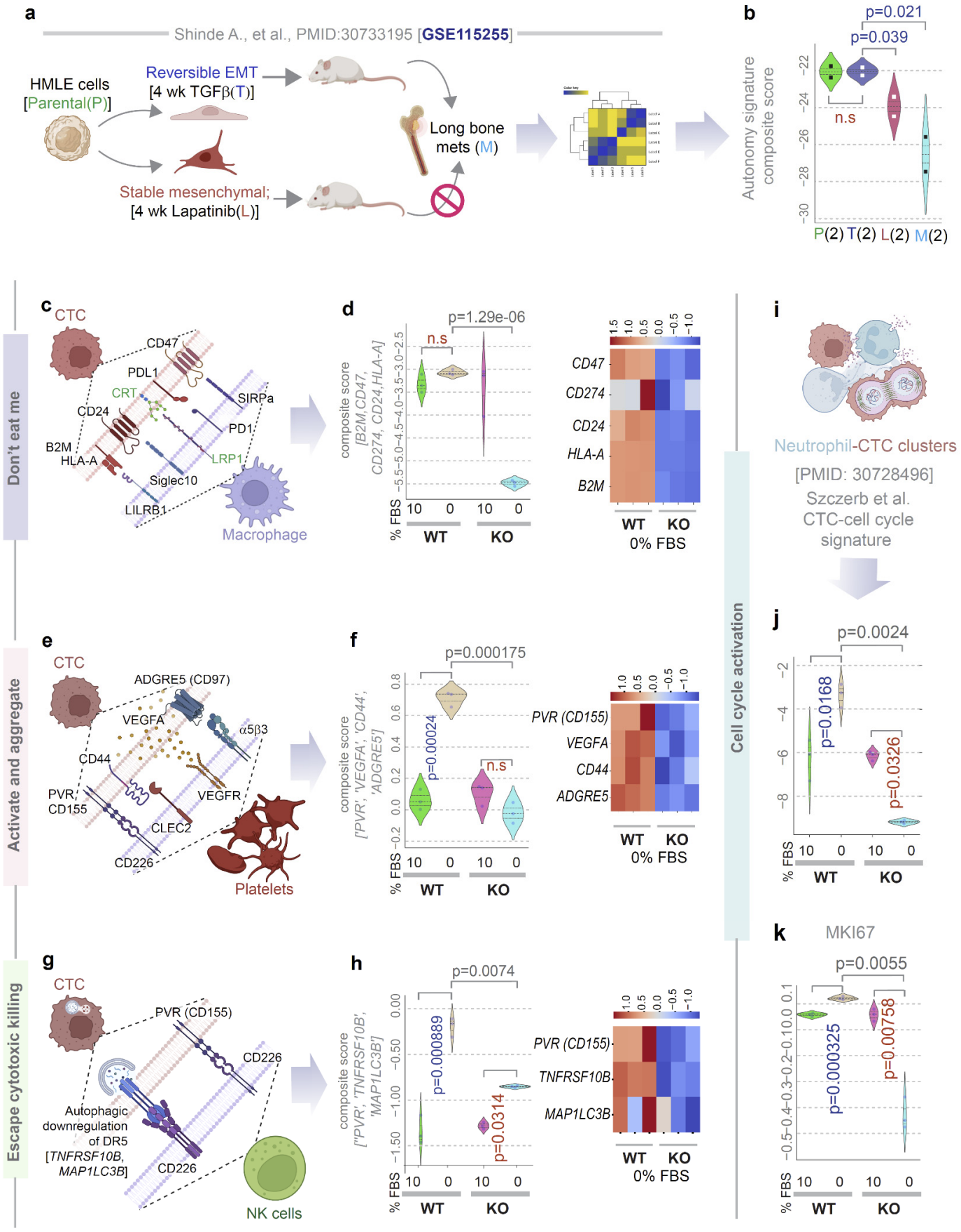

Figure 6. Autonomy is associated with reversible EMT, capacity to evade immune cells and proliferate.

866 **a-b.** Schematic (a) displays the key steps in study design using Her2-transformed mammary epithelial cells
867 (HMLE, parental). Induction of reversible EMT (by TGFβ) but not stable EMT (by Lapatinib) is associated with
868 the development of long-distance metastases to bones (BM). Parental, reversible EMT, stable mesenchymal
869 and bone metastases-derived clones of HMLE cells were subjected to RNA seq. Violin plots (b) display the
870 composite score of the genes in the autonomy signature in the HMLE clones. *p* values based on Welch's T-test,
871 comparing TGFβ-induced reversible EMT and other clones.
872
873 **c-h.** Schematics summarize the paired CTC-macrophage (c), or CTC-platelets (e) or CTC-NK cell (g)
874 components known to enhance the metastatic potential of heterotypic CTC clusters(45). Violin plots (left panels;
875 d, f, h) show the composite score of various markers of immune evasion in CTCs in parental (WT) and GIV-
876 depleted (GIV-KO) MDA MB-231 cells. Heatmaps (right panels; d, f, h) show the expression of each gene. See
877 **Figure S6** for violin plots for the individual genes.

878 **i-k**. Schematic (i) summarizes the study showing cell cycle activation in CTC-neutrophil clusters. Violin plots
879 show either the composite score of expression of genes in that specific CTC-associated cell cycle signature (j)
880 or levels of expression of *MKI67* (k) in parental (WT) and GIV-depleted (GIV-KO) MDA MB-231 cells.

881 *Statistics*: *p* values based on Welch's T-test. Blue and red font for p values indicate, significant up- or
882 downregulation, respectively.

883

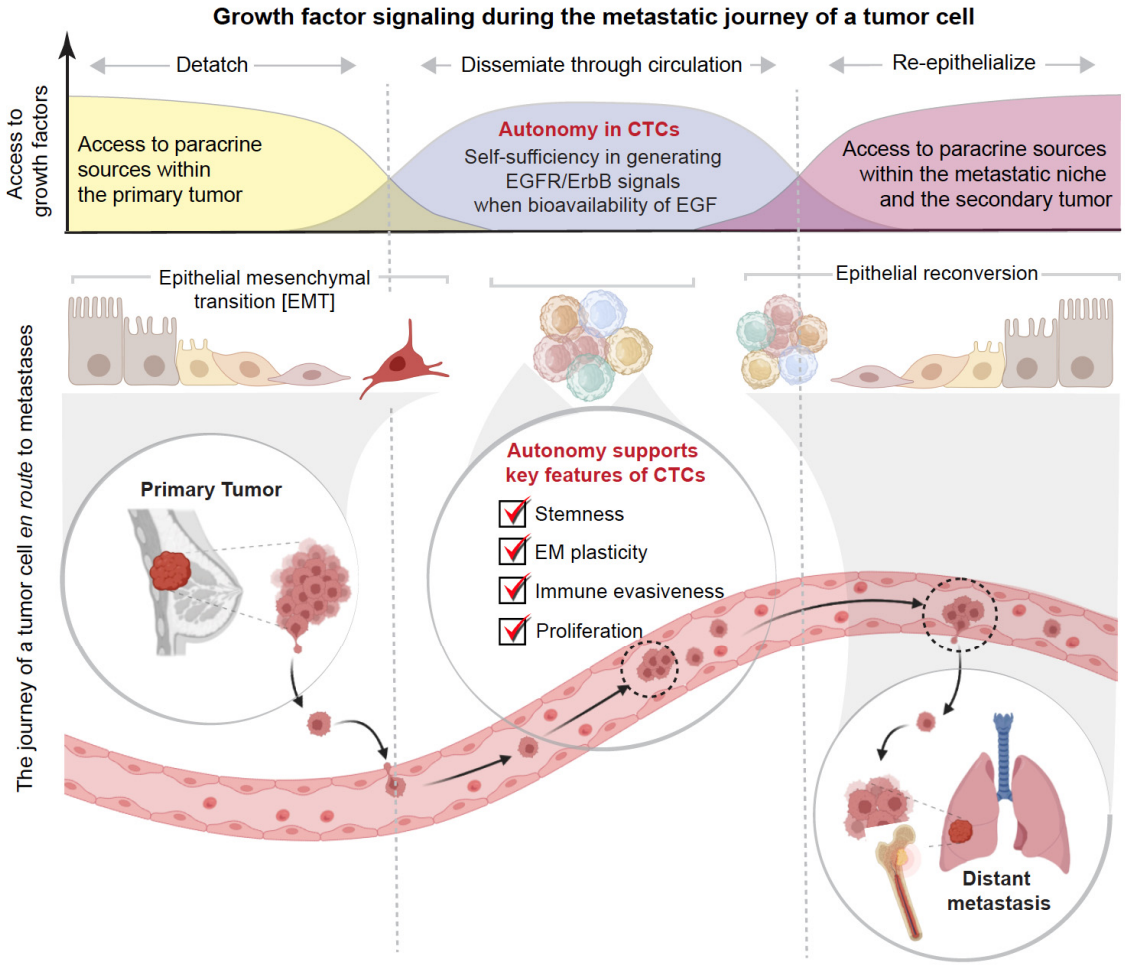

Figure 7. Summary of findings and working model: Schematic showing the various phases of the journey of tumor cells *en route* to seeding metastases. *Top*: Growth factor signaling and source during that journey. *Bottom*: Epithelial to mesenchymal (EMT) and mesenchymal to epithelial (MET) transition states in primary (left) or metastatic (right) tumors and the transitioning state in CTC clusters. Growth signaling autonomy, which is seen in CTCs, appears to support a self-sufficient EGFR/ERBB signaling program that is required for re-epithelialization during metastasis. Other properties of autonomous CTCs include, stemness, EM-plasticity, immune evasiveness, and cell proliferation.